The Astrophysical Journal, 836:186 (17pp), 2017 February 20 https://doi.org/10.3847/1538-4357/aa5b91


# Detection of Time Lags between Quasar Continuum Emission Bands Based On Pan-STARRS Light Curves

Yan-Fei Jiang (姜燕飞)[1], Paul J. Green[2], Jenny E. Greene[3], Eric Morganson[4], Yue Shen[4,5,15], Anna Pancoast[2,16], Chelsea L. MacLeod[2], Scott F. Anderson[6], W. N. Brandt[7,8,9], C. J. Grier[7,8], H.-W. Rix[10], John J. Ruan[6], Pavlos Protopapas[11], Caroline Scott[12], W. S. Burgett[13], K. W. Hodapp[13], M. E. Huber[13], N. Kaiser[13], R. P. Kudritzki[13], E. A. Magnier[13], N. Metcalfe[14], J. T. Tonry[13], R. J. Wainscoat[13], and C. Waters[13]

[1] Kavli Institute for Theoretical Physics, University of California, Santa Barbara, CA 93106, USA
[2] Harvard-Smithsonian Center for Astrophysics, 60 Garden Street, Cambridge, MA 02138, USA
[3] Department of Astrophysical Sciences, Princeton University, Princeton, NJ 08544, USA
[4] Department of Astronomy, University of Illinois at Urbana-Champaign, Urbana, IL 61801, USA
[5] National Center for Supercomputing Applications, University of Illinois at Urbana-Champaign, Urbana, IL 61801, USA
[6] Department of Astronomy, University of Washington, Box 351580, Seattle, WA 98195, USA
[7] Department of Astronomy and Astrophysics, The Pennsylvania State University, University Park, PA 16802, USA
[8] Institute for Gravitation and the Cosmos, The Pennsylvania State University, University Park, PA 16802, USA
[9] Department of Physics, The Pennsylvania State University, University Park, PA 16802, USA
[10] Max Planck Institute for Astronomy, Königstuhl 17, D-69117 Heidelberg, Germany
[11] Institute for Applied Computational Science, John A. Paulson School of Engineering and Applied Sciences, Harvard University, Cambridge, MA 02138, USA
[12] Astrophysics, Imperial College London, Blackett Laboratory, London SW7 2AZ, UK
[13] Institute for Astronomy, University of Hawaii, 2680 Woodlawn Drive, Honolulu HI 96822, USA
[14] Department of Physics, Durham University, South Road, Durham DH1 3LE, UK
*Received 2016 August 25; revised 2017 January 12; accepted 2017 January 13; published 2017 February 21*

## Abstract

We study the time lags between the continuum emission of quasars at different wavelengths, based on more than four years of multi-band ($g$, $r$, $i$, $z$) light curves in the Pan-STARRS Medium Deep Fields. As photons from different bands emerge from different radial ranges in the accretion disk, the lags constrain the sizes of the accretion disks. We select 240 quasars with redshifts of $z \approx 1$ or $z \approx 0.3$ that are relatively emission-line free. The light curves are sampled from day to month timescales, which makes it possible to detect lags on the scale of the light crossing time of the accretion disks. With the code *JAVELIN*, we detect typical lags of several days in the rest frame between the $g$ band and the $riz$ bands. The detected lags are ~2–3 times larger than the light crossing time estimated from the standard thin disk model, consistent with the recently measured lag in NGC 5548 and microlensing measurements of quasars. The lags in our sample are found to increase with increasing luminosity. Furthermore, the increase in lags going from $g - r$ to $g - i$ and then to $g - z$ is slower than predicted in the thin disk model, particularly for high-luminosity quasars. The radial temperature profile in the disk must be different from what is assumed. We also find evidence that the lags decrease with increasing line ratios between ultraviolet Fe II lines and Mg II, which may point to changes in the accretion disk structure at higher metallicity.

*Key words:* accretion, accretion disks – galaxies: active – galaxies: nuclei – quasars: general

*Supporting material:* figure sets, machine-readable table

## 1. Introduction

The optical/ultraviolet continuum emission from active galactic nuclei (AGNs), particularly at high luminosity, is widely believed to be produced by a geometrically thin and optically thick accretion disk around the super-massive black hole (SMBH), where the Eddington ratio for electron scattering opacity is ~0.01–1. With the minimal assumption that the emission is from blackbody radiation with temperature $T$, for Eddington luminosity $L_{\rm Edd}$ and emission area $400\pi\ r_s^2$, where $r_s$ is the Schwarzschild radius, $T \sim (L_{\rm Edd}/(400\pi\sigma_r r_s^2))^{1/4} \sim 1.2 \times 10^5 (M_{\rm BH}/10^8\ M_\odot)^{-1/4}$ K, where $M_{\rm BH}$ is the mass of SMBH and $\sigma_r$ is the Stefan–Boltzmann constant. This is independent of any accretion disk model and consistent with the big blue bump in AGN spectra (Shields 1978; Koratkar & Blaes 1999). The standard thin disk model (Shakura & Sunyaev 1973) is often used to describe the accretion disks in quasars. In this model, the effective temperature $T_{\rm eff}$ changes with radius $R$ as $T_{\rm eff} \propto R^{-3/4}$ for a given black-hole mass and accretion rate. Therefore, radiation at different wavelengths is dominated by emission at different radii.

Because of the large distance of quasars and the small size of their accretion disks, it is not typically possible to resolve the disk directly. For a few quasars, microlensing can be used to constrain the half-light radii of the accretion disks (Morgan et al. 2010; Mosquera et al. 2013; Chartas et al. 2016). Variability is another powerful tool to infer the spatial dimensions of the disks from temporal information (Lawrence 2016), which can be observed easily. By studying the time lags between the light curves of the continuum emission and the broad emission lines in AGNs, the size of the broad line region can be measured, based on the simple assumption that the lag corresponds to the time photons take to travel from the central black hole to the broad line region. This well-established reverberation mapping technique (Blandford & McKee 1982; Peterson 1993) has been applied to many nearby AGNs to study the structure of the broad line region and estimate black-hole masses (e.g., Peterson et al. 2004; Bentz et al. 2009; Shen 2013; Barth et al. 2015; Shen et al. 2016).

[15] Alfred P. Sloan Research Fellow.
[16] Einstein Fellow.

In principle, a similar reverberation mapping technique that measures the lags between the continuum emission in different bands can be used to constrain the structures of accretion disks. However, the main challenge is that the expected light crossing time across different radii in the optical/ultraviolet emission region (particularly the most inner region) of the accretion disk is much smaller than the lags between the continuum emission and most broad emission lines. The light crossing time across the expected radii responsible for the continuum emission at ~10–100 Schwarzschild radii in the rest frame of the quasar is ~0.1–1 day for a $10^8$ $M_\odot$ SMBH, which means that we need regular observations with a cadence comparable to or smaller than a day in order to detect the lags. Accretion disks can also have much longer time lags between different radii in principle. For example, lags caused by the propagation of fluctuations in the accretion process happen on the viscous timescale (Uttley et al. 2003; Marshall et al. 2008). However, this is not as clean as the light crossing timescale for the purpose of constraining accretion disk physics because detailed modeling of these long timescale processes is very uncertain.

The short timescale lags between different bands of the continuum emission have been detected for a few AGNs, including NGC 7496 (Wanders et al. 1997; Collier et al. 1998), Markarian 79 (Breedt et al. 2009), NGC 4051 (Breedt et al. 2010), NGC 3783, MR2251-178 (Lira et al. 2011), NGC 2617 (Shappee et al. 2014), NGC 5548 (McHardy et al. 2014), NGC 4395 (McHardy et al. 2016), and NGC 6814 (Troyer et al. 2016), and upper limits of 14 AGNs by Sergeev et al. (2005). Recently, significant lag detections across a wide range of continuum emission bands have been found for NGC 5548 (Edelson et al. 2015; Fausnaugh et al. 2016). Most of these detections show that the short wavelength bands lead the long wavelength bands, which is usually interpreted as irradiation of the outer disk by the X-rays produced near the black hole (Krolik et al. 1991; Cackett et al. 2007). Interestingly, the inferred sizes of the optical emitting regions are systematically larger than the predicted values from standard thin disk models by factors of ~2–3 (Lawrence 2012; Edelson et al. 2015; Fausnaugh et al. 2016), which is also consistent with the results based on the microlensing measurements (Chartas et al. 2016).

Theoretically, the standard thin disk model has led to many puzzles when it is used to describe observations of AGNs in the regime, where it is supposed to apply (e.g., Koratkar & Blaes 1999). The radiation pressure dominated inner region of this model, where most of the continuum radiation is emitted, is thermally unstable (Shakura & Sunyaev 1976; Jiang et al. 2013). However, the expected large amplitude fluctuations in the thermal timescale caused by the instability (Janiuk et al. 2002) have never been observed for most AGNs. Modifications of the standard thin disk models have been proposed to explain these discrepancies, including the large temperature fluctuation model of Dexter & Agol (2011), and reprocessing of the far-UV radiation by optically thick clouds (Gardner & Done 2016). Recently, Jiang et al. (2016) proposed that the iron opacity bump may play an important role in determining the thermal properties and structure of AGN accretion disks. The previous continuum lag detections for a few AGNs are not sufficient to determine the statistical properties of the lags and test the predictions of these models. The goal of this paper is to measure the lags between different continuum bands for a much larger sample of AGNs, which will enable us to quantify the distributions of the lags and see how the lags change with other properties of AGNs.

In Section 2, we describe the data and the sample we select. The method we use to measure the lags is described in Section 3. Our main results are described in Section 4. Finally, in Section 5, we discuss the implications of our results on the understanding of accretion physics and necessary future work.

## 2. Observational Data and Sample Selection

### 2.1. The Pan-STARRS1 Medium Deep Fields

We have chosen to study quasars in the Medium Deep Fields of the Pan-STARRS1 (PS1) survey, because of their depth and large numbers of imaging epochs. The PS1 survey used a wide-field $f/4.4$ optical telescope system designed for survey mode operation at the Haleakala Observatory on the island of Maui in Hawaii. The system, with 1.8 m primary and 0.9 m secondary mirrors, produces a 3.3 $deg^2$ field of view in combination with the PS1 gigapixel camera (GPC1). The 1.4 Gpixel detector is composed of a mosaic of 60 CCD chips each of 4800 × 4800 pixels with each 10 $\mu$m pixel spanning $0\farcs258$ on the sky through five main broadband filters denoted as $g_{P1}$, $r_{P1}$, $i_{P1}$, $z_{P1}$, $y_{P1}$. The PS1 photometric system is described in Tonry et al. (2012), and passband shapes are detailed in Stubbs et al. (2010). The $y_{P1}$ band data typically have fewer points compared with data in other bands and are not used in the following analysis.

While the main 3$\pi$ survey observed three-fourths of the sky north of −30° decl. in about a dozen epochs from 2010 May until 2014 March, the Medium Deep Field (MDF) survey of PS1 was designed to provide deeper exposures with many more epochs in selected fields, with multiple observations in all five filters each season, taken when the airmass was lower than 1.3. One MDF cycle starts with 8 × 113 s exposures in the $g_{P1}$ and $r_{P1}$ bands on the first night, with 8 × 240 s in the $i_{P1}$ band the second night, and finally 8 × 240 s in the $z_{P1}$ band the third night, before the cycle recommences. Any one filter/epoch consists of eight dithered exposures of either 8 × 113 s for $g_{P1}$ and $r_{P1}$ or 8 × 240 s for the other three, giving nightly stacked images of 904 s and 1920 s duration.

The raw science frames exposed with the PS1 telescope were reduced by the PS1 Image Processing Pipeline conducting standard procedures of image calibration, source detection, astrometry, and photometry. We use an updated version of the "ubercalibrated" PS1 data from Schlafly et al. (2012), which includes the PS1 data up through PV1 (using PV1 of the PS1 pipeline) and is calibrated absolutely to 0.02 mag or better. This database excludes detections flagged by PS1 as cosmic rays, edge effects, and other defects. We consider only nine PS1 MD fields (1, and 3–10) that overlap the SDSS footprint. The median number of PS1 epochs is 284, 340, 406, 445, and 179 in the $g$, $r$, $i$, $z$, $y$ filters, respectively, and median magnitudes are in the range of $16 < i_{P1} < 21.5$. As determined by the analysis of non-variable stars in Morganson et al. (2015), the magnitude uncertainties delivered by the PS1 pipeline have been inflated, by 1.387, 1.327, 1.249, 1.228, and 1.170 for *g, r, i, z, y*, respectively.

### 2.2. The Parent Quasar Sample

We began by searching for all objects within 1°.5 of each MDF central coordinate that have been observed and spectroscopically classified as quasars within SDSS Data Release 10

(part of SDSS-III; Eisenstein et al. 2011; Pâris et al. 2014) by querying the CasJobs data server. This yielded 2421 unique quasars.

We also included quasars identified in two ancillary pilot programs using the multi-fiber Baryon Oscillation Spectroscopic Survey (BOSS) spectrograph within SDSS-III (Dawson et al. 2013). The SDSS-III program approved spectroscopy of variables and X-ray source counterparts within MD01 and MD03, as a pilot study for two spectroscopic subprograms of eBOSS proposed (and currently underway) for SDSS-IV: SPectroscopic IDentification of E-Rosita Sources (SPIDERS) is for X-ray source follow-up, and the Time Domain Spectroscopic Survey (TDSS) is for classification and study of photometric variables. Both programs are briefly described in Alam et al. (2015). Despite the reference to eROSITA, SPIDERS sources actually were selected optical counterparts to cataloged *ROSAT* and/or *XMM-Newton* X-ray sources. The TDSS pilot variable candidates were selected from early PS1 MDF ubercalibrated (Schlafly et al. 2012) photometry, when typically about a third of the final number of epochs was available. TDSS pilot candidate variable priorities were assigned from a weighted sum of variability features $R_{CS}$, SNR and the median SDSS-PS1 magnitude difference across the *griz* bands. SNR in each filter is defined as the ratio of the 75%–25% magnitude quartiles divided by the median magnitude error derived from the full light curve. $R_{CS}$ is the range of a cumulative sum from Ellaway (1978). These statistical features and their use are described in Kim et al. (2011).

For MD01, plate number 6369 was observed for a total of 75 minutes on 2012 October 13 (MJD 56217), while for MD03, plate 6369 was observed for a total of 60 minutes on 2012 December 23 (MJD 56284). We include all the quasars spectroscopically identified in the MD01 and MD03 pilot campaigns, both by the SDSS pipeline and as confirmed from our own visual inspection. We note that, given the X-ray and optical photometric variability selection, the quasar samples in these two fields therefore have a somewhat different set of selection biases than the usual SDSS optical color quasar selection algorithms. We further include all 991 spectroscopic quasars known within MD07, of which 849 are targeted in an ongoing campaign of repeated spectroscopy for reverberation mapping there (Shen et al. 2015). Before completion of this paper, all the included quasar spectra have become available to the public via SDSS Data Release 12.

Since we are interested in understanding the physics of accretion in our sample, we seek to analyze only quasars for which spectroscopy allows a reasonable estimate of the SMBH mass, using the single-epoch virial method described by Shen et al. (2011).

Across all nine MDFs, we identified 3178 unique quasars that have $M_{\rm BH}$ fits and PS1 MDF light curves that pass all of our criteria. The $M_{\rm BH}$ measurements have been performed with different broad emission-line fits, depending on which lines are available in the SDSS spectrum as a function of quasar redshift. For $z < 0.76$, we choose to use H$\beta$ and $\lambda_0$ 5100 Å continuum, with $k_{\rm Bol} = 9.26$. For $0.76 < z < 2.1$, we use Mg II and $\lambda_0$ 3900 Å, continuum with $k_{\rm Bol} = 5.15$. For $2.1 < z < 3.18$, we use C IV and $\lambda_0$ 1350 Å, continuum, with $k_{\rm Bol} = 3.81$. The fit errors are generally lower for spectra with higher signal-to-noise ratios, which is markedly higher (typically $\sim$30 pixel$^{-1}$) within MD07, because we fit spectra of 32 co-added observation epochs obtained for the reverberation mapping campaign (Shen et al. 2015).

### 2.3. The Final Quasar Sample

Broad emission-line fluxes are known to vary in response to continuum flux variations, but with a time delay related to their physical distance from the continuum-emitting region. While this effect is exactly what allows the reverberation mapping method, we are seeking to detect shorter delays that may occur between continuum-emitting regions. The existence of broad emission lines in the broadbands may contaminate the possible lags between continuum emissions in standard lag analysis (Chelouche & Zucker 2013). Therefore, from the larger sample of quasars with SDSS spectra, black-hole mass estimates, and PS1 light curves, we select for further analysis those quasars in redshift ranges where broad emission lines present the least contribution within the PS1 broadband filter transmission curves (particularly *g* band), yielding 51 quasars with $0.16 < z < 0.42$ and 189 with $0.95 < z < 1.1$. All the quasars in our sample and their properties are summarized in Table 1.

Distributions of the estimated luminosity, black-hole mass and Eddington ratio for our sample are shown in Figure 2. The sample covers a luminosity range from $\sim 3 \times 10^{43}$ to $10^{47}$ erg s$^{-1}$ and the estimated black-hole masses range from $10^7$ to $10^{10}$ $M_\odot$. As expected, the low-redshift quasars also typically have lower luminosity.

One common way to quantify the level of variability in the light curves is the normalized excess variance $\sigma^2_{\rm rms}$ (Nandra et al. 1997; Vaughan et al. 2003), which is basically the standard deviation of the measurement error corrected flux scaled by the mean flux and it is calculated according to Equation (1) of Simm et al. (2016). In order to minimize the effects of light-curve gaps, we calculate the excess variance in each season and take the average value of $\sigma^2_{\rm rms}$ over the four seasons. The distributions of $\sigma^2_{\rm rms}$ for the *g*-band light-curve of our sample are also shown in Figure 2. The normalized excess variance shows an anti-correlation with luminosity and with black-hole mass, which can also be captured by a single anti-correlation between $\sigma^2_{\rm rms}$ and Eddington ratio $L/L_{\rm Edd}$, with $\sigma^2_{\rm rms} \propto (L/L_{\rm Edd})^{-0.20\pm0.11}$. The Pearson and Spearman *p*-values of the anti-correlation, which are the probability that $\sigma^2_{\rm rms}$ is not correlated with $L/L_{\rm Edd}$, are $3.0 \times 10^{-4}$ and $3.8 \times 10^{-4}$ respectively. A similar anti-correlation between the overall (long-term) variability amplitude and $L/L_{\rm Edd}$ has been found by other studies (Wilhite et al. 2008; Bauer et al. 2009; Ai et al. 2010; MacLeod et al. 2010; Ponti et al. 2012).

## 3. Lag Analysis Method

Cross-correlation is the traditional method to calculate lags between two light curves (e.g., Peterson et al. 1998). This method works well for well-sampled light-curves and it does not assume any model for the continuum light curve. However, cross-correlation interpolates between the data points, so it may not be easy to pick out lag signals from light curves with large and irregular gaps. This is the case for our data. Example light-curves for two quasars in MD01 and MD03 are shown in Figure 3. The Pan-STARRS light curves typically have cadences varying from a day to a few months with large gaps between seasons. For this reason, we use JAVELIN (Zu et al. 2011, 2016) to calculate the lags between different bands.

**Table 1**
Sample Summary

| SDSS Name | R.A. (Deg) | Decl. (Deg) | $z$ | $m_g$ (mag) | $m_r$ (mag) | $m_i$ (mag) | $m_z$ (mag) | $\log L$ (erg s$^{-1}$) | $\log M_{\rm BH}$ $M_\odot$ | $\sigma^2_{\rm rms}$ |
|---|---|---|---|---|---|---|---|---|---|---|
| J022303.23–025713.8 | 35.7635 | −2.9539 | 0.41 | 19.36 ± 0.01 | 19.39 ± 0.01 | 19.26 ± 0.02 | 18.89 ± 0.04 | 45.09 | 7.81 | 8.68e–06 |
| J022115.53–025843.4 | 35.3147 | −2.9787 | 0.99 | 20.91 ± 0.03 | 20.85 ± 0.05 | 20.78 ± 0.06 | 20.70 ± 0.19 | 45.20 | 8.20 | 2.61e–05 |
| J021809.24–035848.7 | 34.5385 | −3.9802 | 0.98 | 21.95 ± 0.08 | 21.78 ± 0.09 | 21.49 ± 0.10 | 21.47 ± 0.40 | 45.08 | 7.27 | 1.92e–05 |
| J021800.49–040649.2 | 34.5021 | −4.1137 | 1.04 | 21.15 ± 0.04 | 20.86 ± 0.04 | 21.00 ± 0.07 | 20.43 ± 0.18 | 45.17 | 7.95 | 2.75e–05 |
| J022616.01–030537.0 | 36.5667 | −3.0936 | 0.99 | 21.41 ± 0.05 | 21.10 ± 0.06 | 21.32 ± 0.10 | 20.77 ± 0.23 | 44.95 | 0.00 | 2.41e–05 |
| J022808.90–035845.3 | 37.0371 | −3.9792 | 0.99 | 21.93 ± 0.07 | 21.55 ± 0.08 | 21.40 ± 0.10 | 21.92 ± 0.53 | 44.10 | 7.50 | 1.46e–05 |
| J022521.25–032628.5 | 36.3386 | −3.4413 | 1.07 | 20.68 ± 0.03 | 20.17 ± 0.03 | 20.42 ± 0.05 | 20.09 ± 0.10 | 45.39 | 8.51 | 3.71e–05 |
| J022659.82–035015.0 | 36.7493 | −3.8375 | 0.29 | 20.97 ± 0.03 | 20.20 ± 0.03 | 19.99 ± 0.03 | 19.49 ± 0.07 | 44.57 | 7.31 | 1.24e–05 |

(This table is available in its entirety in machine-readable form.)

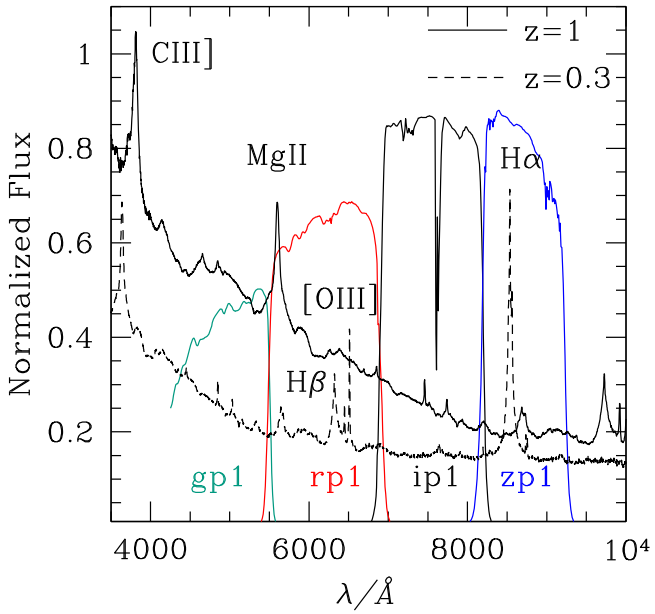


**Figure 1.** Pan-STARRS broadband filters as given by Tonry et al. (2012) and typical quasar spectrum at redshifts 1 and 0.3 from Telfer et al. (2002).

### 3.1. Fitting Procedure with JAVELIN

Because quasar variability is found to be acceptably described by the damped random-walk (DRW) model (Kelly et al. 2009; Kozłowski et al. 2010; MacLeod et al. 2010), which is a first-order continuous autoregressive model, JAVELIN first fits a DRW model to the $g$-band data to get the variability amplitude $\sigma$ and the damping timescale $\tau$. The model is then smoothed and shifted to fit the $r$ and $i$ bands simultaneously. The lags between the $g-r$ and $g-i$ bands are determined when best fits for the three bands are achieved. We have also confirmed that if we fit the $g-r$ and $g-i$ bands independently, the signals we find are consistent with the previous case within the uncertainty of the peaks. We repeat the process to calculate the lag between the $g$ and $z$ bands. For each quasar, we carry out 90,000 Monte Carlo Markov Chain (MCMC) burn-in and sampling iterations to estimate the probability distributions of lags and other parameters of DRW models. In our sample, there are 40 quasars (labeled as *noLag*) where JAVELIN cannot find a significant lags in this approach (see discussion Section 5). This leaves 37 quasars between $z=0.16$ and 0.42 and 163 between $z=0.95$ and 1.1 with detected signals (labeled as *iLD*), which will be the focus of our analysis.

Notice that although JAVELIN was originally developed to calculate lags between the continuum and lines, we can easily replace the lines with continuum emission in different bands, since the different continuum bands should, at least to first-order approximation, follow the same variability process but with a delay. In fact, JAVELIN has been successfully used to calculate continuum–continuum lags in NGC 5548 (Fausnaugh et al. 2016), where it agrees with the cross-correlation methods well for these well-sampled light curves.

### 3.2. Testing JAVELIN

The irregular cadence and the fact that not all bands are observed simultaneously can introduce artificial lag signals in principle. We have done a series of experiments to test the effects of the cadence on the lag signals detected by JAVELIN.

The first set of experiments gives JAVELIN pairs of light curves without any lag signals. We calculate the mean magnitude $\mu_0$ and standard deviation $\sigma_m$ in the $r$, $i$, and $z$ bands. We take the time of each data point in these bands but assign a magnitude $\mu_0+\sigma_m s$, where $s$ is a normally distributed random variable. The error on each data point is constructed in the same way based on the mean and standard deviation of the error bars of the original data. In this way, we construct mock light curves in the $r$, $i$, and $z$ bands using the actual cadence but uncorrelated magnitudes. We feed JAVELIN the actual $g$-band data and these mock light curves to calculate the lags following the same procedures as we have described before. The resulting probability density distribution is usually uniformly distributed over all the possible lags. However, some common spurious lags show up. Two examples are shown in Figure 4. These lags are usually located at special locations for different quasars in the same field such as −40, −15, 15, and 40 days, which are likely caused by the cadence of the observations as similar values also show up in the probability density distribution of cadences. This may also explain similar lag signals we see in some quasars when we calculate the lags using the actual data. We emphasize that we never see any artificial signals around timescales of a few days in this experiment. To test the effects of different noise models, we have also constructed four independent DRW light curves, which are mapped to the actual MJDs in $g$, $r$, $i$, $z$-bands. Error bars of the original data are assigned to these mock light curves. We find very similar results as in the case when we use white noise mock light curves.

To see whether JAVELIN is able to detect genuine lags based on the Pan-STARRS light curves, we generate mock light curves with specified lags. We first take the actual $g$-band

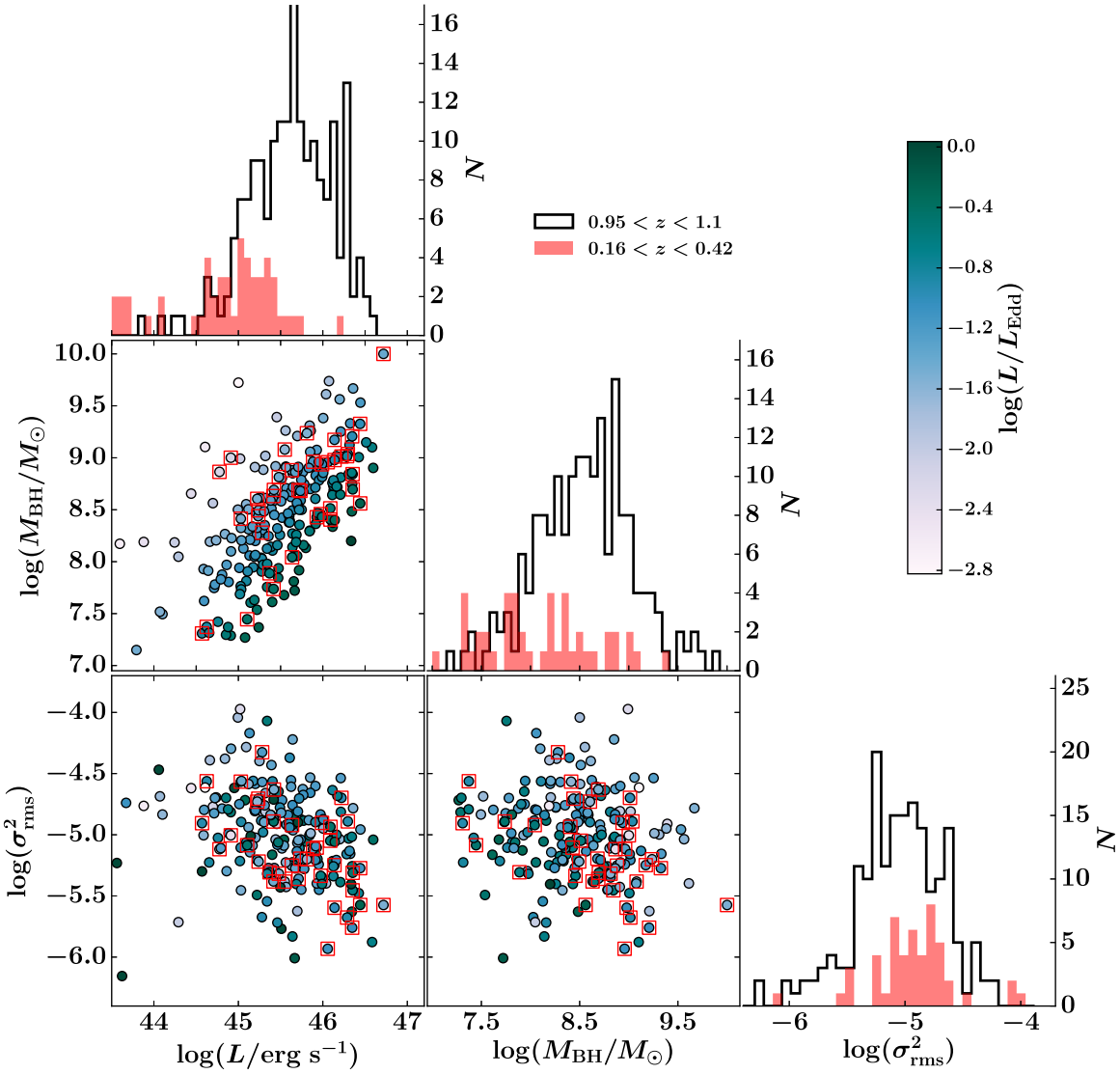


**Figure 2.** Distributions of the estimated bolometric luminosity $L$, black-hole mass $M_{\rm BH}$, and normalized $g$-band excess variance $\sigma^2_{\rm rms}$ for the 200 quasars with detected lags. Each quasar is color coded by Eddington ratio. The 39 quasars with significant detections (subsample *cLD*) are labeled by the open red squares. The diagonal panels are the histograms of $L$, $M_{\rm BH}$, and $\sigma^2_{\rm rms}$ in the two redshift bins.

light curve and add 2, 5, and 10 days, respectively, to the time of each data point to make three mock light curves. The magnitude and error on each data point in the mock light curves are the same as in the original data. These mock light curves are then mapped to the actual MJDs in $r$ band via linear interpolation. This effectively introduces 2, 5, and 10 day lags (in the observed frame) in the mock light curves. We provide JAVELIN with the actual $g$-band data and the mock light curves as three data sets to calculate the lags. Probability distributions of the lags in this experiment for quasar J022020.02–034331.1 are shown in Figure 5. The peaks of the calculated lags from JAVELIN are located at the locations of the input signals, except for the case with a lag of 10 days, where the probability density distribution peaks at 12 days with a standard deviation 2.2 days. The large uncertainty and offset in this case are likely due to the interplay between the input signal and the light-curve cadences. The lag distributions are also typically broader for quasars with larger magnitude uncertainties. This experiment shows that JAVELIN is able to pick out lags as short as two days (in the observed frame) even given the irregular cadence of the Pan-STARRS light curves.

We also perform similar experiments with mock light curves for different bands based on the DRW model. We generate a DRW light curve using the best-fit parameters (the damping timescale $\tau$ and variation amplitude $\sigma$) as returned by JAVELIN for the $g$-band data. This light curve is uniformly sampled with cadence 0.05 day and covers the full time interval of the $g$-, $r$-, $i$-, and $z$-band data. We generate mock light curves by interpolating the high-cadence light curve at the observation times of the data points in each band. In this way, we get the same light curve sampled at different MJDs in the four bands. Error bars on the mock light-curve magnitudes in each band are taken to be the mean error bar of the actual light curve in the same band. We have also tried using the actual errors from the original light curves, which do not show any difference. We then shift the high-cadence light curve by 1 to 13 days and map to $r$, $i$, and $z$ bands. We use JAVELIN to calculate the lags between the $g$ band and 13 shifted light curves resampled in the $r$, $i$, and $z$ bands. Figure 6 shows examples of the calculated

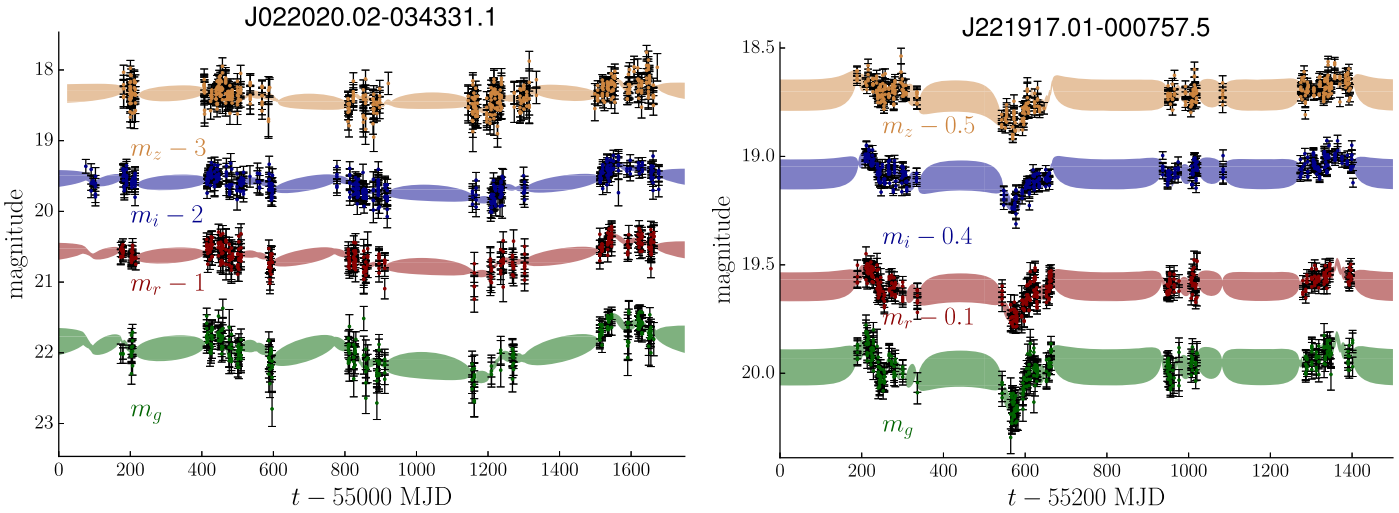


**Figure 3.** Example light-curves in the *g*, *r*, *i*, and *z* bands for the two sample quasars J022020.02–034331.1 in MD01 and J221917.01–000757.5 in MD09. The shaded region is the weighted mean of JAVELIN light curves that are consistent with the data and the $1\sigma$ dispersion of those light curves. Light curves for the full sample with JAVELIN fits are available online.

(The complete figure set (200 images) is available.)

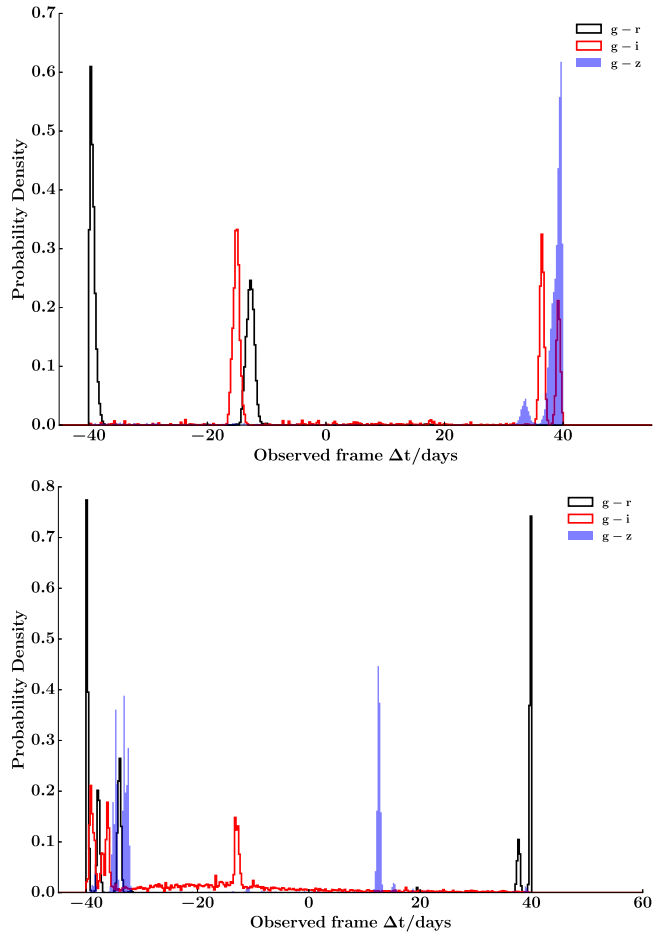


**Figure 4.** Probability density distributions of lags in the observed frame between the actual *g*-band data and randomly generated mock light curves in *r*, *i*, and *z* bands as described in Section 3.2. The top panel is for quasar J022020.02–034331.1 in MD01, while the bottom panel is for quasar J221917.01–000757.5 in MD09.

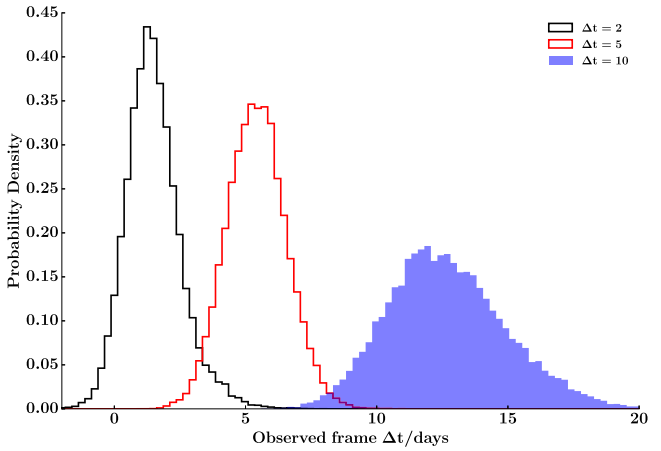


**Figure 5.** Probability density distributions of the lags in the observed frame as calculated by JAVELIN between the actual *g*-band data and the shifted light curves with 2, 5, and 10 days as described in Section 3.2. This example is for quasar J022020.02–034331.1 in MD01.

lags for two quasars. JAVELIN recovers the lags we inserted between the *g* band and the other bands in all cases, though the uncertainty is clearly larger compared with the previous experiment. In some cases, as shown in the top panel of Figure 6, when the input lag is around 10 days, artificial negative lags around −15 to −20 days show up. This is likely caused by the combination of the input signal and the cadence because these artificial signals only show up with input signals around 10 days and they are usually located at −10 to −20 days. We have also checked that we never see any spurious lags around timescales of a few days in this experiment.

The mock light curves generated in the above experiments correspond to the case with a $\delta$ transfer function. In order to test the effects of a finite width in the transfer function, we generate new mock light curves by convolutions between the high-cadence DRW light curve and a log-normal transfer function (Starkey et al. 2016) $f(\Delta t) = \exp[-(\log(\Delta t) - \mu)^2/(2\sigma^2)]/((2\pi)^{1/2}\sigma\Delta t)$. This effectively introduces a mean lag $\Delta t = \exp[\mu + \sigma^2/2]$ in the mock light curves, while $\sigma$ determines the width of the transfer function. We have tried $\sigma = 0.1$, 0.2, 0.5 and in each case we generate

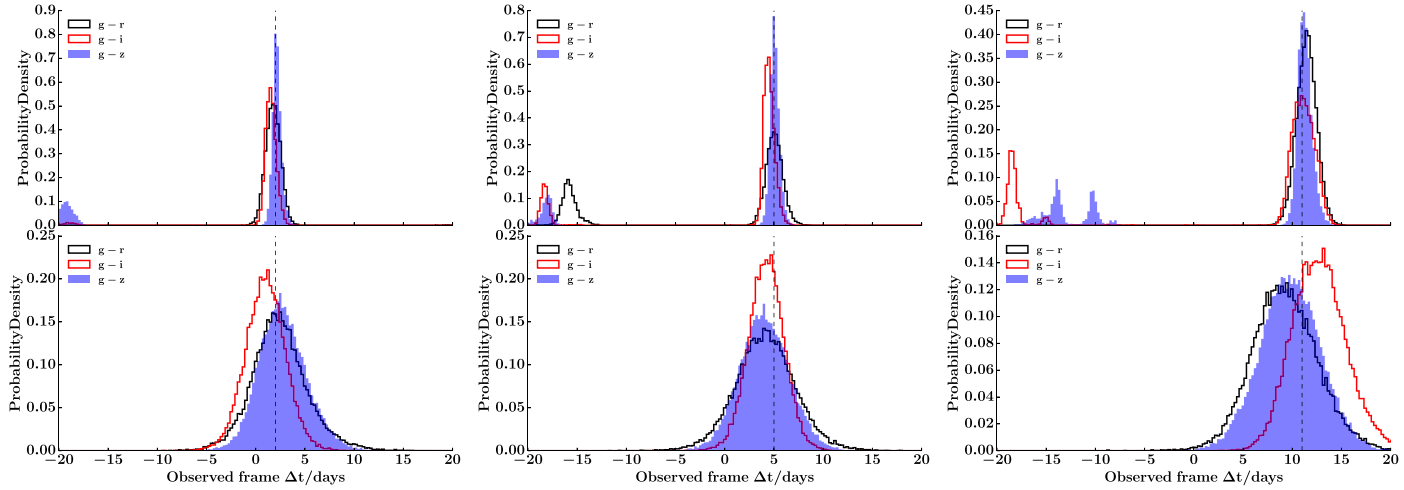


**Figure 6.** Probability density distributions of lags in the observed frame between the mock $g$ band light-curve and shifted and resampled mock $r$-, $i$-, and $z$-band light curves. The mock light curves are constructed based on a high-cadence damped random-walk light curve as described in Section 3.2. From left to right, they are cases when the mock $r$-, $i$-, and $z$-band light curves are shifted by 2, 5, and 11 days, respectively, as indicated by the vertical dashed lines. The bottom panels are for quasar J022020.02–034331.1 in MD01, while the top panels are for quasar J221917.01–000757.5 in MD09. The mean $g$-band magnitude uncertainties for J221917.01–000757.5 and J022020.02–034331.1 are 0.01 and 0.09 mag, respectively, which explains why the probability density distributions in the bottom panel are much broader than the distributions in the top panels.

mock light curves with $\mu = \log(2) + \sigma^2$, $\log(5) + \sigma^2$, $\log(10) + \sigma^2$. These mock light curves are mapped to $r$, $i$, and $z$ bands and we feed them to JAVELIN to calculate the lags with respect to the $g$-band mock light curve. We carry out this experiment for the same two quasars as in Figure 6. JAVELIN is still able to recover the mean lag values as in Figure 6. However, the uncertainty is significantly increased with larger $\sigma$. In the case of $\sigma = 0.5$, full width at half maximum (FWHM) of the probability density distribution is increased by a factor of ∼2–2.5 compared to the results from the previous experiment.

The damping timescale $\tau$ we get by fitting DRW models to the light curves of quasars in our sample varies from 30 to 500 days. We have also tried the experiment of forcing $\tau$ to be larger than 200 days in JAVELIN, which is the typical value found for most quasars (MacLeod et al. 2010), and we find almost identical lag signals. This demonstrates that the DRW parameters we get from JAVELIN may not be robust, but the lags we aim to detect are.

### 3.3. Test of the Cross-correlation Method

In order to assess how well the cross-correlation method is able to identify lags given the sampling of our light curves, we have also tried this method following the procedure described in Peterson et al. (2004) with the same mock light curves as in the last section. We calculate the standard cross-correlation function (CCF) with linear interpolation between data points for mock light curves in two different bands. The centroid of the CCF is calculated for points with cross-correlation coefficients larger than 80% of the peak value of CCF. We use 50,000 independent realizations of the light curves to estimate the cross-correlation centroid distribution, which corresponds to the probability distribution of the lags. An updated "flux randomization/random subset selection" (FR/RSS) method (Peterson et al. 1998; Welsh 1999) that accounts for the redundant selections by reducing the flux uncertainties by the square root of the number of multiple selections is used to estimate the centroid distribution. Figure 7 shows the results for the same mock light curves of quasar J022020.02–034331.1 as used in the bottom panel of Figure 6. Although the mock $r$-, $i$-, and $z$-band light curves are shifted by 2, 5, and 11 days respectively, the cross-correlation method is unable to pick out the signals with the cadences of our Pan-STARRS light curves. Even if we only calculate CCF for the light curves in each season and average the results of all the seasons to avoid the large seasonable gaps, the cross-correlation method still cannot reproduce the input lags. In contrast, JAVELIN succeeds at this test, as shown in Figure 6. Thus, we will only focus on the results calculated by JAVELIN.

### 3.4. Emission Lines

Our sample has also been observed spectroscopically (Shen et al. 2015), which allows us to quantify the contamination of lines in our sample and study the relation between the lags and various line equivalent widths (see Section 5).

In our analysis of the inter-band lags, we only use one DRW model to describe the light curve in each band. If there are broad emission lines contributing a significant fraction of the flux in each band, they can affect the lags between the continuum radiation in different bands we try to measure (Chelouche & Zucker 2013; Edelson et al. 2015; Fausnaugh et al. 2016), because they have different lags with respect to the continuum radiation. Although we have chosen two special redshift ranges to minimize the contamination, Figure 1 shows that there are still some major lines in the bands, particularly blended Fe II and Mg II in $g$ band and Mg II and H$\beta$ in $r$ band, that can potentially contaminate the lag signals.

In both the $g$ and $r$ bands, the ratio between the line and continuum fluxes is always smaller than 10% in our sample with a median value of 1% in the $g$ band and 3% in the $r$ band. For the subsample *cLD* (see Section 4.1), the ratio is always smaller than 5.8% with a median value of 0.47% in the $g$ band and 3.2% in the $r$ band. Given the small ratio of line to continuum flux, in general, the broad lines cannot significantly affect the lags we detect (Fausnaugh et al. 2016).

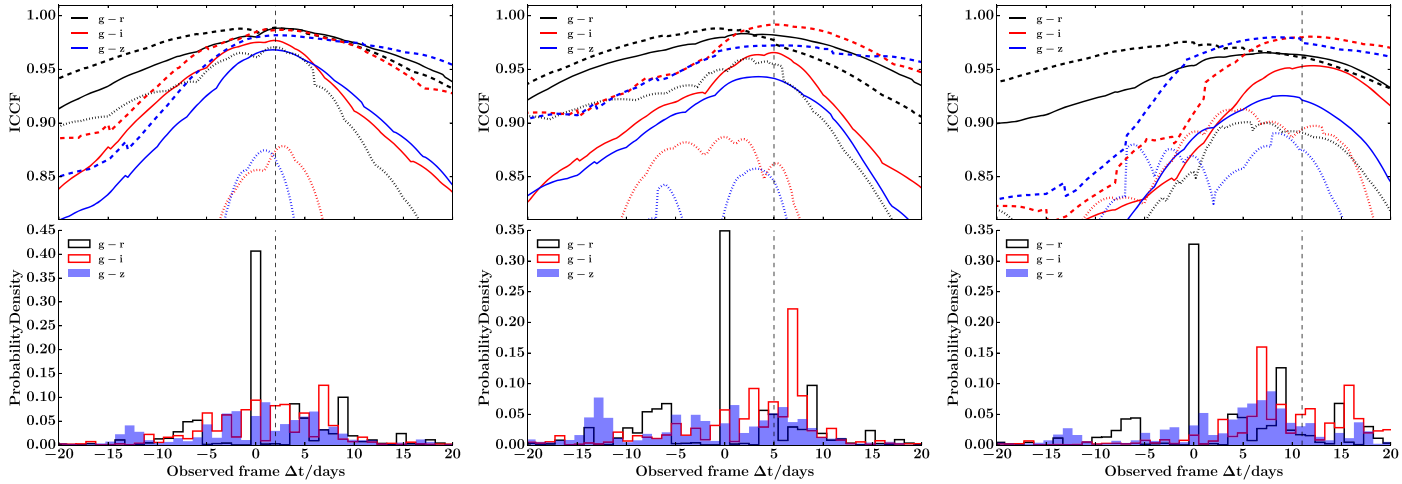


**Figure 7.** Top: interpolated cross-correlation coefficient (ICCF) between the mock $g$- and $r$-, $i$-, $z$-band light-curves. The solid lines use all the data points, while the dashed and dotted lines are based on the first or second half of the data, to show the variations in the ICCF. Bottom: probability density distributions of lags calculated based on the centroid of ICCF as described in Section 3.3. This experiment is done for quasar J022020.02–034331.1 as in the bottom panel of Figure 6. From left to right, the mock $r$-, $i$-, and $z$-band light curves are shifted by 2, 5, and 11 days as indicated by the vertical dashed line.

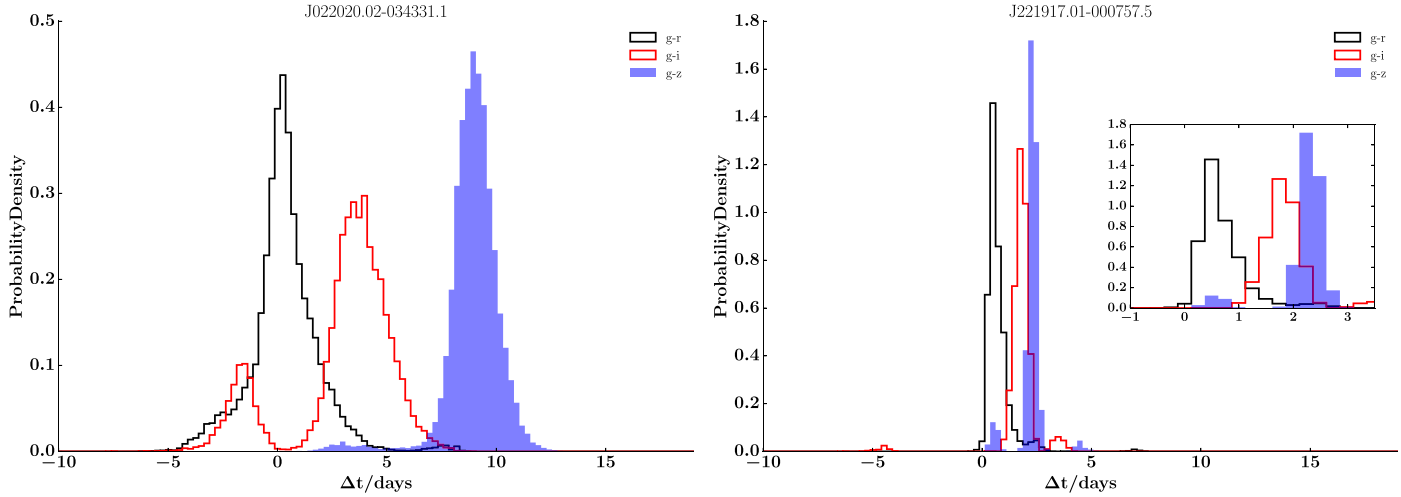


**Figure 8.** Example histograms of the rest frame lags between $g$, $r$, $i$, and $z$ bands for the quasars J022020.02–034331.1 in MD01 and J221917.01–000757.5 in MD09. The small window in the right panel is the zoomed in plot between −1 and 3.5 days. The two examples show cases with significantly detected lags. Histograms of rest frame lags for all quasars are available online.

(The complete figure set (200 images) is available.)

## 4. Results

### 4.1. Lags for the Whole Sample

From our original sample of 240 quasars, JAVELIN is able to fit DRW models and show probability density distributions of lag signals with Gaussian shapes for 200 quasars (subsample *iLD*). We have also done the Anderson–Darling test to make sure the fitting residuals do follow the Gaussian distributions. However, not every quasar shows strong and consistent variability across the four bands, which is necessary for JAVELIN to detect significant lags between the $g$ band and other bands. Figure 8 shows two examples of the probability density distributions of the lags for quasars J022020.02–034331.1 and J084536.18+453453.6 with significantly detected signals. There is only a single dominant peak in each case, which is very similar to the experiment shown in Figure 6. The lags between the $g$ band and other bands increase with increasing wavelength. For examples like this, we take the FWHM, corresponding to $2.35\sigma$ for Gaussian distributions, as the uncertainty in the lag. The lag is calculated as the centroid of the distribution, which is the probability density weighted mean lag in the region with probable density larger than half of the maximum value.

As quasars in each MDF have the same cadence, it is interesting to assess whether the 40 quasars (named subsample *noLag*) for which *JAVELIN* cannot detect any lag signal have any property that is significantly different from the others. The structure function (e.g., MacLeod et al. 2010; Choi et al. 2014; Kozłowski 2016), which quantifies variability as a function of timescale, is a useful quantity to show differences in variability properties across the sample. We first calculate the structure functions for the $g$, $r$, $i$, $z$-band light curves for each quasar according to the procedure described in Kozłowski (2016). The structure function typically reaches a maximum value around the damping timescale $\tau$ as in the DRW model. For time

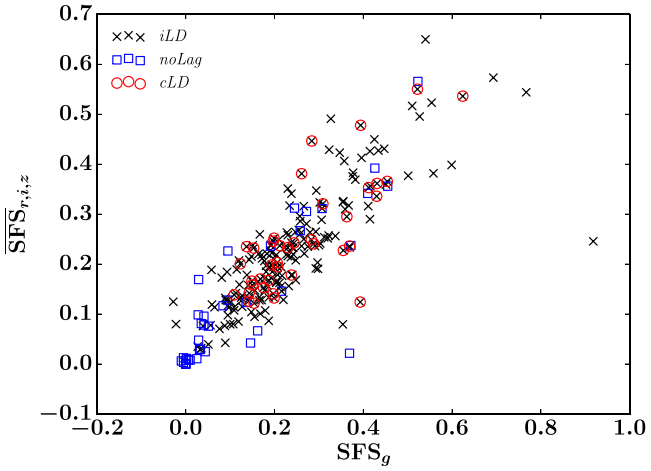


**Figure 9.** Distributions of structure function slope (SFS) for the $g$-band light curves and the mean SFS for light curves in $r$, $i$, $z$ bands. The black crosses, red circles, and blue squares are for samples *iLD*, *cLD*, and *noLag*, respectively, as explained in Table 2.

differences smaller than $\tau$, the structure function is well-fit by a power law, the slope of which tells us how the variability amplitude changes from short to long timescales.

If the light curves have strong noise at timescales smaller than the few day timescales in which we are interested, the power-law slope will be shallow and the DRW models will have difficulty fitting the short timescale fluctuations and finding a lag. If the $r$, $i$, $z$-band light curves follow the $g$-band light-curves with a fixed lag, we also expect them to have a similar structure function slope (SFS). We calculate $\mathrm{SFS}_g$, $\mathrm{SFS}_r$, $\mathrm{SFS}_i$, and $\mathrm{SFS}_z$ for subsamples *iLD*, *noLag*, and *cLD* (the last will be defined below). Figure 9 shows the distribution between $\mathrm{SFS}_g$ and the mean slope $\overline{\mathrm{SFS}}_{r,i,z} \equiv \sqrt{(\mathrm{SFS}_r^2 + \mathrm{SFS}_i^2 + \mathrm{SFS}_z^2)/3}$. Most of the quasars in *noLag* are indeed located at the bottom left corner with small $\mathrm{SFS}_g$ and $\overline{\mathrm{SFS}}_{r,i,z}$, although they have similar structure function normalizations. This means that their structure functions are flatter and their light-curves have more variability/noise on short timescales. We have also checked that these quasars do not have any special properties in terms of black-hole mass, luminosity, or normalized excess variance compared with the other quasars.

For the other 200 quasars, where *JAVELIN* detects a lag, there are 102 quasars showing single dominant peaks between the $g - r$, $g - i$, and $g - z$ bands while the rest have multiple peaks distributed in a wide range from $-40$ days to 40 days. The two groups of quasars do not show any significant differences in the key parameters $L$, $M_{\mathrm{BH}}$, $\sigma^2_{\mathrm{rms}}$ compared with each other. They also have similar ratios between the magnitude uncertainties and magnitudes. If we require that lags increase from $g - r$, $g - i$ to $g - z$ bands, as they would if the lags are caused by reprocessing of radiation from the center, we find 39 quasars in our sample (named subsample *cLD*). The physical properties of this subsample are shown by the open red squares in Figure 2. They span the whole parameter space of the original sample, and again do not show any systematic difference compared to *iLD* in their luminosity, black-hole mass or normalized excess variance distributions. The median luminosity of this subsample is $5.4 \times 10^{45}$ erg s$^{-1}$, which is consistent with the median luminosity of the whole sample.

**Table 2**
Sample Statistics

| Name | No. | $0.95 < z < 1.1$ | $0.16 < z < 0.42$ |
|---|---|---|---|
| Initial Sample | 240 | 189 | 51 |
| *noLag* | 40 | 29 | 11 |
| *iLD* | 200 | 160 | 40 |
| *cLD* | 39 | 34 | 5 |

**Note.** JAVELIN does not detect any lag signal from the subsample named *noLag*. The subsample *iLD* has lag detections, while *cLD* is the subsample with single significantly peaked lags and lags increase with increasing wavelength differences.

For the other 63 quasars that have single dominant peaks but do not show a progression in time lag for the redder bands, 23 quasars have both $g - i$ and $g - z$ lags smaller than $g - r$ lags, while 20 quasars only have $g - i$ lags smaller than $g - r$ lag and 11 quasars only have $g - z$ lags smaller than $g - r$ lags. There are also 9 quasars showing both $g - i$ and $g - z$ lags larger than $g - r$ lags but with $g - z$ lags smaller than $g - i$ lags. The numbers of quasars for the initial sample and subsamples *noLag*, *iLD*, *cLD* are summarized in Table 2.

### 4.2. The Stacked Signals

In order to see the properties of lags for the whole sample, we stack the signals in the following way. We divide the lag interval from $-20$ to 20 days into 160 bins with bin width 0.25 day. For each quasar, we count the number of MCMC samples yielding the rest frame lag in each bin. We then calculate the median value of the MCMC counts for the whole sample for each bin, which gives the probability distribution of the stacked lags for the whole sample. We repeat the process for the $g - r$, $g - i$, and $g - z$ lags. Because each quasar has the same number of total MCMC trials, all quasars are given the same weight, thus building up the distribution of most likely lag for the sample as a whole. Probability density distributions of the rest frame lags stacked in this way are shown in the top panel of Figure 10.

The probability density weighted mean lags for the $g - r$, $g - i$, and $g - z$ bands are $1.1 \pm 1.5$, $2.1 \pm 1.9$, and $3.0 \pm 1.9$ days in the rest frame with the quoted uncertainties being the standard deviation and most of the lag signals being positive. The mean lags increase from $g - r$ to $g - z$ bands, though they are still consistent within one standard deviation. Differences between the mean $g - r$, $g - i$, and $g - z$ lags should be proportional to the distances between the radii where $g$, $r$, $i$, and $z$ photons are expected to be emitted, which will be discussed in Section 4.5 in detail. The stacked signals have broad distributions and multiple peaks, particularly for the $g - i$ and $g - z$ lags. This is partially because quasars in our sample have a wide range of luminosities and black-hole masses, as shown in Figure 2. Another reason is that apart from the *cLD* subsample, individual quasars do not have single peaked and well ordered lags, which will contribute to the noise in the stacked profile. In order to see whether the stacked signals are dominated by the subsample *cLD* or not, we have repeated the same stacking experiment excluding the quasars in the *cLD* subsample. We find very similar stacked signals as

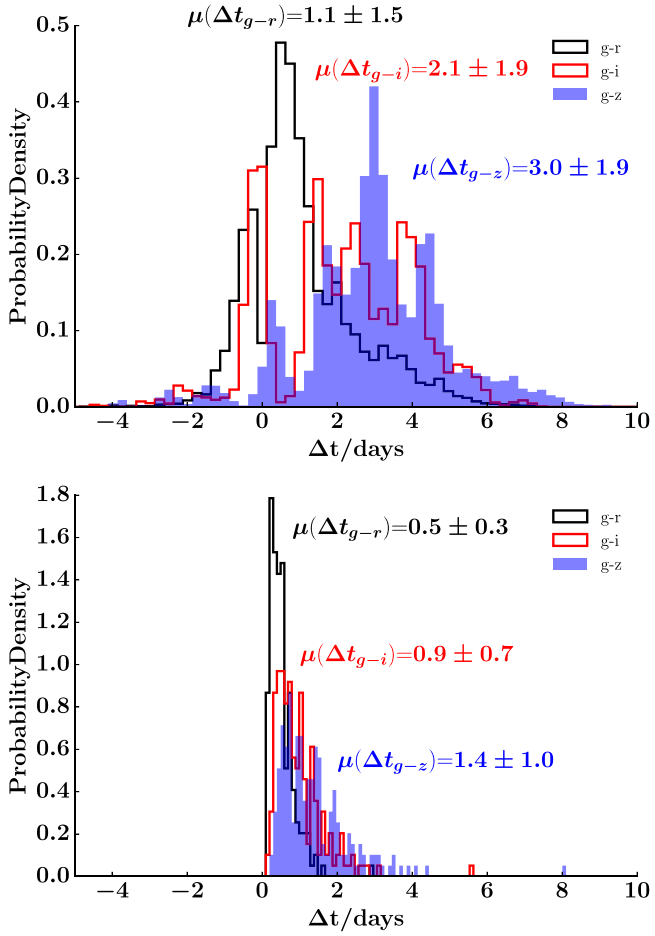


**Figure 10.** Top: stacked histograms of lags between $g$ and $r$, $i$, $z$ bands for the whole sample. The lags are measured in the rest frame of the quasars. The probability density is normalized such that the total area under each histogram is one. The averaged lags for each histogram are labeled in the figure. Bottom: histograms of the theoretically estimated lags between $g$ and $r$, $i$, $z$ bands based on the standard thin disk model as described in Section 4.5, using the estimated black-hole mass and bolometric luminosity for each quasar.

shown in Figure 10, which suggests that the results represent properties of the whole sample.

### 4.3. Dependence of Lags on Luminosity

If the detected lags are related to the light-travel time across different radii of the accretion disks, they should vary with the luminosity and black-hole mass of the quasars, since these determine the sizes of accretion disks. The increase of the inter-band lags with increasing luminosity has also been noticed by Sergeev et al. (2005) based on observations of 14 AGNs. We check for luminosity dependence by dividing the whole sample into two subsamples, one with luminosity smaller than the median value $3.7 \times 10^{45}\,\mathrm{erg\,s^{-1}}$ and the other one with luminosity larger than this value. We stack the quasars in each luminosity bin as described in Section 4.2. The mean lags between the $g$ band and the $r$, $i$, and $z$ bands for the lower luminosity subsample are 0.5 ± 1.3, 0.7 ± 1.8, and 2.1 ± 2.8 days, respectively, while the corresponding mean lags for the higher luminosity subsample are 2.0 ± 1.6, 3.8 ± 1.3, and 3.3 ± 1.4 days. The mean lags do increase with luminosity as expected, though the uncertainty is large for the stacked signals of the whole sample. The $p$ values of Kolmogorov–Smirnov (KS) test for the null hypothesis that the subsamples with high and low luminosities are from the same distributions for $g-r$, $g-i$, and $g-z$ lags are $6 \times 10^{-10}$, $2 \times 10^{-25}$, and $2 \times 10^{-4}$, respectively, which supports the conclusion that the two subsamples are significantly different.

**Table 3**
Rest Frame Lags for the Subsample *cLD*

| SDSS Name | $\Delta t_{g-r}$ days | $\Delta t_{g-i}$ days | $\Delta t_{g-z}$ days |
|---|---|---|---|
| J022659.82–035015.0 | −0.13 ± 1.75 | 1.50 ± 1.00 | 2.98 ± 2.00 |
| J022144.75–033138.8 | 4.27 ± 1.00 | 7.34 ± 0.75 | 13.75 ± 0.25 |
| J022020.02–034331.1 | 0.15 ± 1.25 | 3.81 ± 2.25 | 9.08 ± 1.75 |
| J022340.29–042852.4 | −0.11 ± 3.25 | 1.74 ± 1.50 | 1.73 ± 3.50 |
| J084536.18+453453.6 | 0.40 ± 0.75 | 6.78 ± 1.00 | 11.95 ± 3.25 |
| J084512.99+445208.9 | 2.11 ± 1.75 | 4.59 ± 2.25 | 4.46 ± 1.50 |
| J083841.70+430519.0 | 1.09 ± 0.25 | 1.59 ± 0.25 | 5.91 ± 0.25 |
| J084610.76+452153.1 | 2.18 ± 0.75 | 5.38 ± 0.25 | 5.34 ± 0.75 |
| J084341.41+444023.3 | 0.10 ± 1.75 | 1.12 ± 0.75 | 10.05 ± 1.50 |
| J083756.22+431713.4 | −0.83 ± 1.75 | 5.81 ± 1.00 | 8.97 ± 1.00 |
| J083836.14+435053.3 | 3.49 ± 2.50 | 5.87 ± 0.75 | 12.63 ± 0.75 |
| J083425.01+442658.2 | −0.02 ± 1.00 | 1.03 ± 0.50 | 2.22 ± 1.50 |
| J084517.64+441004.9 | 0.75 ± 0.25 | 3.25 ± 0.25 | 4.65 ± 0.25 |
| J095701.58+023857.3 | 5.30 ± 0.50 | 6.40 ± 0.25 | 9.00 ± 0.25 |
| J100029.15+010144.8 | −0.25 ± 0.25 | 1.50 ± 0.25 | 2.00 ± 0.25 |
| J100421.01+013647.3 | 2.36 ± 2.75 | 4.60 ± 0.25 | 12.10 ± 0.75 |
| J100327.67+015742.4 | 4.15 ± 0.75 | 3.99 ± 0.50 | 8.89 ± 0.25 |
| J100025.24+015852.0 | −0.00 ± 0.50 | 4.00 ± 0.25 | 7.84 ± 0.25 |
| J122549.28+472343.7 | 0.61 ± 0.25 | 2.38 ± 0.25 | 2.65 ± 0.25 |
| J142336.76+523932.8 | 0.07 ± 0.75 | 4.01 ± 1.00 | 11.66 ± 0.75 |
| J141104.86+520516.8 | 5.51 ± 1.00 | 6.73 ± 0.50 | 14.16 ± 0.75 |
| J141018.04+523446.0 | 2.96 ± 1.50 | 3.97 ± 0.50 | 7.38 ± 0.25 |
| J140739.16+525850.7 | 0.75 ± 0.25 | 3.51 ± 0.50 | 10.50 ± 0.25 |
| J141147.59+523414.5 | −1.50 ± 0.50 | 0.88 ± 1.25 | 4.37 ± 0.25 |
| J141539.59+523727.9 | −0.62 ± 0.25 | 1.75 ± 0.25 | 2.75 ± 0.25 |
| J142008.27+521646.9 | 3.35 ± 0.25 | 7.00 ± 0.25 | 6.86 ± 0.25 |
| J141138.06+534957.7 | 0.75 ± 0.50 | 3.21 ± 1.00 | 3.54 ± 0.50 |
| J141811.34+533808.5 | 0.23 ± 3.00 | 2.01 ± 2.00 | 3.16 ± 3.75 |
| J141358.90+542705.9 | −0.20 ± 1.00 | 2.89 ± 3.25 | 3.61 ± 1.75 |
| J141856.19+535844.9 | 2.09 ± 0.25 | 9.25 ± 0.25 | 14.34 ± 0.25 |
| J142106.26+534406.9 | −0.75 ± 0.50 | 7.00 ± 0.25 | 11.89 ± 0.25 |
| J221504.35+010935.2 | 2.61 ± 5.25 | 5.05 ± 6.25 | 10.86 ± 1.75 |
| J221434.82+001923.9 | −0.25 ± 1.50 | 1.01 ± 0.50 | 3.27 ± 2.50 |
| J221447.75–002032.7 | 3.35 ± 0.25 | 4.73 ± 1.00 | 6.36 ± 0.75 |
| J221917.01–000757.5 | 0.59 ± 0.25 | 1.78 ± 0.50 | 2.36 ± 0.25 |
| J222228.39+002640.6 | 1.17 ± 2.00 | 5.65 ± 0.75 | 8.78 ± 1.00 |
| J232826.57+010207.8 | 2.26 ± 0.50 | 5.24 ± 0.50 | 6.12 ± 0.75 |
| J232907.12+003416.6 | 1.70 ± 1.50 | 4.25 ± 0.50 | 6.51 ± 1.00 |
| J233201.42–005655.2 | 3.50 ± 1.50 | 5.76 ± 0.50 | 6.23 ± 0.50 |

**Note.** Properties of these lags are discussed in Figures 12, 14, and 15.

### 4.4. Lags for the cLD Subsample

Lags for the 39 *cLD* quasars with significant, well ordered lag detections are summarized in Table 3. We repeat the same stacking process for this subsample to look for the mean lags between different bands, which is shown in the top panel of Figure 11. The probability density weighted mean $g-r$, $g-i$, and $g-z$ lags for the subsample are 1.2 ± 1.2, 3.6 ± 1.5, and 5.3 ± 1.8 days. The lags between the $g$ and $r$ bands are almost the same as the stacked lags for the whole sample, while lags between $g$ and $i$, $z$ bands become larger. The probability density of negative lags for $g-i$ and $g-z$ bands is almost zero for this subsample. This subsample will be the

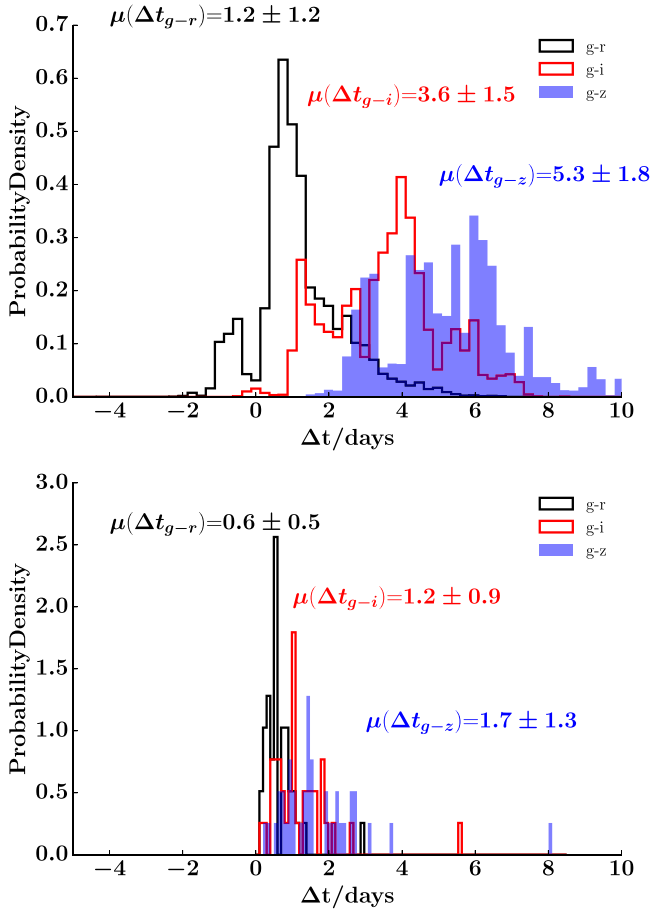


**Figure 11.** Top: stacked histograms of lags between $g$ and $r$, $i$, $z$ bands for the selected subsample *cLD*. Bottom: histograms of the theoretically estimated lags between $g$ and $r$, $i$, $z$ bands for this subsample.

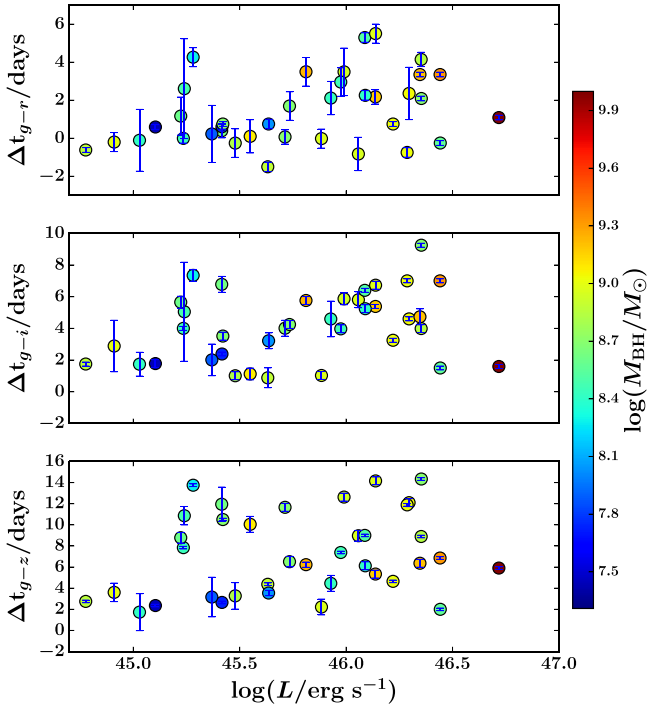


**Figure 12.** Distributions of lag with luminosity for the 39 *cLD* quasars with significant, consistent detections. Each data point is color coded by the estimated black-hole mass. From top to bottom, the three panels are rest frame lags between $g - r$, $g - i$, and $g - z$ bands respectively. The dashed black lines in each panel indicate 0 lags.

focus of the analysis in the following sections, mainly because only they can be compared with simple reprocessing models to constrain the physics of accretion disks individually.

Distributions of the lags as a function of luminosity and black-hole mass for the 39 *cLD* quasars are shown in Figure 12. There is a weak trend whereby the lags increase with increasing luminosity, though the scatter is large. The Pearson correlation coefficients between luminosity and $g - r$, $g - i$, $g - z$ lags are 0.41, 0.35, and 0.24 with corresponding $p$ values 0.0088, 0.028, and 0.14, while the Spearman correlation coefficients between luminosity and the three lags are 0.39, 0.33, and 0.24, respectively, with corresponding $p$ values 0.014, 0.042, and 0.14. Here the $p$ values represent the probabilities that luminosity does not correlate with the lags. Least-squares fits to the lags and luminosities in log–log space (with negative lags excluded) give $\Delta t_{g-r} \propto L^{0.55\pm0.37}$, $\Delta t_{g-i} \propto L^{0.16\pm0.16}$, and $\Delta t_{g-z} \propto L^{0.14\pm0.15}$. These fits are consistent with Sergeev et al. (2005) for the $g - r$ lags but show weaker dependence for $g - i$ and $g - z$ lags.

To quantify the trend with luminosity, we divide the 39 quasars into two subsamples based on the median luminosity and repeat the stacking experiment as before for each subsample. The median luminosities for the two subsamples are $2.11 \times 10^{45}$ and $1.38 \times 10^{46}$ erg s$^{-1}$. Probability density profiles of the lags between the $g$ band and the $r$, $i$, $z$ bands for the two subsamples are shown in the left panel of Figure 13. For the low- and high-luminosity subsamples, the mean lags between the $g$ and $r$, $i$, $z$ bands are $0.3 \pm 1.1$, $2.1 \pm 1.5$, and $3.8 \pm 2.0$ days and $2.8 \pm 1.2$, $4.7 \pm 1.1$ and $6.0 \pm 1.2$ days, respectively, where the error bars represent the standard deviation of the lags in the stacked probability density distributions. The $p$ values of KS the test for the null hypothesis that the subsamples are from the same distributions for $g - r$, $g - i$, and $g - z$ lags are $4 \times 10^{-6}$, $4 \times 10^{-6}$, and $2 \times 10^{-5}$ respectively. This clearly shows that the averaged detected lags of the high-luminosity quasars are significantly larger than lags detected for the low-luminosity quasars.

### 4.5. Comparison with the Standard Thin Disk Model

In the standard thin disk model (Shakura & Sunyaev 1973), the effective temperature at each radius is determined by the local dissipation rate and it changes with radius $R$ as $R^{-3/4}$ for a fixed black-hole mass and accretion rate. If irradiation from the inner region of the disk contributes significantly to the local heating rate, the temperature profile may change.

Following Fausnaugh et al. (2016), we assume the effective temperature $T$ changes with radius $R$ as

$$T(R) = \left(f_i \frac{3GM_{\rm BH}\dot{M}}{8\pi\sigma R^3}\right)^{1/4}, \quad (1)$$

where $f_i$ is a factor that accounts for the irradiation from an X-ray/UV source near the black hole by changing the normalization of the temperature profile, $\sigma$ is the Stefan–Boltzmann constant, $G$ is the gravitational constant, and $\dot{M}$ is the mass-accretion rate. The photon wavelength $\lambda$ is related to the characteristic temperature $T$ as $T = hc/(Xk_{\rm B}\lambda)$, where $h$ and $k_{\rm B}$ are the Planck and Boltzmann constants, $c$ is the speed of light, and $X = 2.49$ (Fausnaugh et al. 2016) is a factor

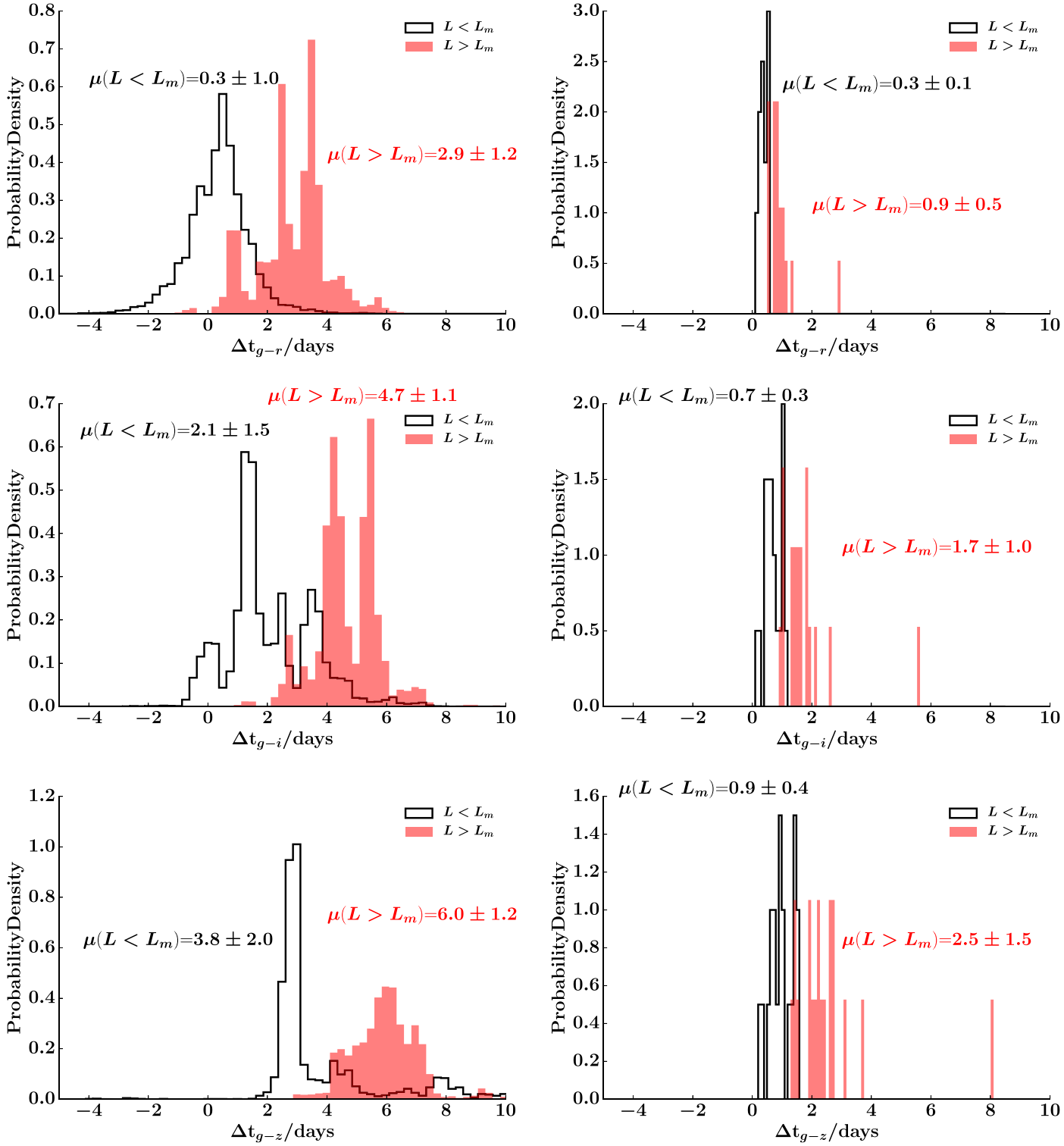


**Figure 13.** Left: stacked histograms of the lags between the $g$-band and the other bands, when the 39 *cLD* quasars with significant, consistent lag detections are divided into two subsamples based on the median luminosity $L_m$. The solid black line is the subsample with $L < L_m$, while the dashed red line is the subsample with $L > L_m$. Right: histograms of the theoretically estimated lags between the $g$ and other bands for the two subsamples divided by luminosity in the same way. From top to bottom, the three rows are for lags between $g - r$, $g - i$, and $g - z$ bands respectively.

to account for emission at this wavelength from a range of temperatures. The central wavelengths of Pan-STARRS $g$, $r$, $i$, $z$ bands are 4750, 6250, 7550, and 8700 Å, which are converted to rest frame wavelengths using the redshift of each quasar. Based on these relations, the median values of the radii in the accretion disks corresponding to these wavelengths for our sample are $17.8r_s$, $25.7r_s$, $33.0r_s$, and $39.9r_s$, respectively, where $r_s \equiv 2GM_{\rm BH}/c^2$ is the Schwarzschild radius. Notice that the distances between neighboring bands are roughly equal in this simple model. The light travel time across two different

radii where photons with wavelengths $\lambda_g$ and $\lambda_x$ are emitted are

$$\Delta t_{g-x} = \left(X\frac{k_{\rm B}\lambda_g}{hc}\right)^{4/3}\left(f_i\frac{3GM_{\rm BH}\dot{M}}{8\pi\sigma}\right)^{1/3} \times\left[\left(\frac{\lambda_x}{\lambda_g}\right)^{4/3}-1\right]. \quad (2)$$

For each quasar, we calculate the mass-accretion rate based on the bolometric luminosity and estimated black-hole mass, assuming a radiative efficiency of 10%. Then we stack the theoretically calculated lags with $f_i = 1$ for simplicity (see discussion Section 5) for the whole sample and compare with our detected lags, which are shown in the bottom panel of Figure 10. The same calculation is also done for the 39 *cLD* quasars and the stacked profiles are shown in the bottom panel of Figure 11. It is clear that the theoretically calculated lags are always smaller than the detected lags by a factor of two for $g-r$ lags and a factor of three for $g-i$ and $g-z$ lags. We also do the same calculations for the luminosity subsamples, which are shown in the right panel of Figure 13. The theoretically calculated lags indeed increase with increasing luminosity in our sample. However, they are always smaller than the detected lags, except for the $g-r$ lags in the low-luminosity subsample, where the lags are not well constrained.

Temperature profiles of the disk in the radial range $\sim 18r_s - 40r_s$ can also be constrained by comparing $\Delta t_{g-i}$, $\Delta t_{g-z}$ with $\Delta t_{g-r}$. According to Equation (2), the three lags should be linearly proportional to each other as

$$\Delta t_{g-i} = \frac{(\lambda_i/\lambda_g)^{4/3}-1}{(\lambda_r/\lambda_g)^{4/3}-1}\Delta t_{g-r},$$
$$\Delta t_{g-z} = \frac{(\lambda_z/\lambda_g)^{4/3}-1}{(\lambda_r/\lambda_g)^{4/3}-1}\Delta t_{g-r}. \quad (3)$$

For the fixed wavelength ratios between $r$, $i$, $z$ band and $g$ band, the slopes are only determined by the radial profile of effective temperature, which is three-fourths in the standard thin disk model. The slopes are independent of black-hole mass, luminosity, accretion rate, and redshift, which only determine the actual values of the lags. The relations between the lags for the subsample *cLD* and the theoretically calculated lags are shown in Figure 14. Compared with the actual lags, the theoretically predicted relation falls systematically on one side of the data. The best fitted relations between bands are $\Delta t_{g-i} \propto \Delta t_{g-r}^{0.25\pm0.13}$ and $\Delta t_{g-z} \propto \Delta t_{g-r}^{0.08\pm0.17}$, where the error bars are for the 95% confidence level. This is significantly flatter compared to the theoretically expected linear relation. If we force a linear relation between the lags, the best fittings are $\Delta t_{g-i} = (0.72\pm0.28)\Delta t_{g-r} + (3.08\pm0.71)$ and $\Delta t_{g-z} = (0.98\pm0.64)\Delta t_{g-r} + (5.86\pm1.42)$, where the theoretical slopes should be 1.94 and 2.81 respectively.

The differences in the correlations point either to a different temperature profile than we assume here, or a different relationship between lags and $M_{\rm BH}$ and $\dot{M}$, particularly as the $g-r$ lag gets larger (corresponding to high-luminosity quasars). A flatter temperature profile and larger apparent disk size are both natural consequences of the model proposed by Lawrence (2012), where the radiation is reprocessed by some cold, thick clouds (see also Gardner & Done 2016). However, alternative pictures, such as strong outflow from the inner region of the accretion disks (Laor & Davis 2014), can also explain the apparently larger light crossing time and flatter temperature profile.

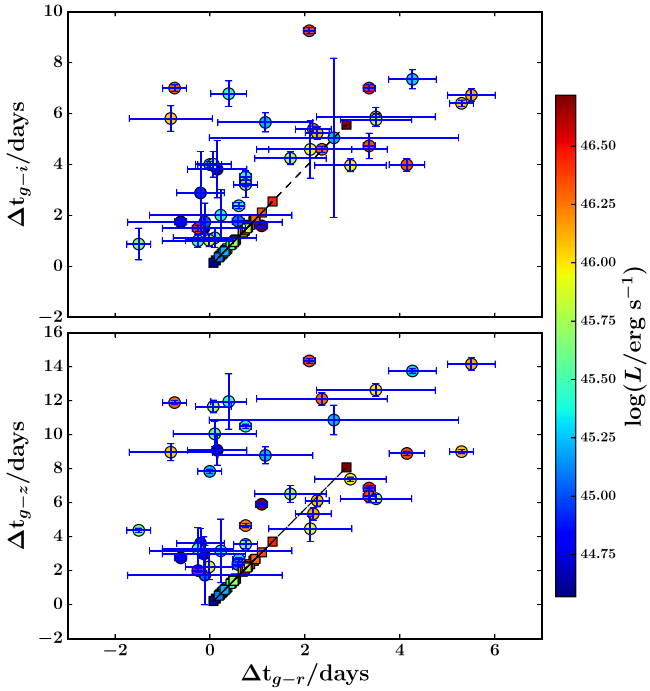


**Figure 14.** Distributions of $g-r$ lags for the subsample *cLD* with respect to $g-i$ (top panel) and $g-z$ (bottom panel) lags. Each data point is color coded with the bolometric luminosity. The filled squares connected by the dashed lines are theoretically calculated lags according to Equation (2).

## 5. Discussions

### 5.1. Comparison with the Lags in NGC 5548

It is interesting to compare our results with the well-studied NGC 5548 (Edelson et al. 2015; Fausnaugh et al. 2016). Because we only have four bands, we cannot constrain the radial temperature profile of the disks over a wide range of wavelengths for each quasar, as in NGC 5548. Instead, we can compare the detected and theoretically expected lags in similar wavelength ranges. NGC 5548 is at redshift 0.017 with the best estimated black-hole mass $\sim 5.2\times10^7\,M_\odot$ (Fausnaugh et al. 2016). If we match the rest frame wavelength at $z=1$ for the majority of our sample with NGC 5548, the Pan-STARRS $g$, $r$, $i$, $z$ bands corresponds to a wavelength range of 2375 Å to 4350 Å for NGC 5548. The reported lag between UVM2 (wavelength 2246 Å) and B band (wavelength 4392 Å) for NGC 5548 is 0.88 day (Edelson et al. 2015), while the theoretically expected lag according to Equation (2) is 0.34 day, if we assume the accretion rate is 10% of the Eddington accretion rate. This is consistent with what we find for our sample in that the detected lag is larger than the theoretically expected lag by a factor of 2.6.

### 5.2. Lags with Unexpected Order

A majority of the quasars show the short wavelength band leading the long wavelength bands with positive $g-r$, $g-i$, and $g-z$ lags. On average, the lags are consistent with variabilities propagating outward via irradiation of the outer disk by the highly variable central radiation. Peaks in the

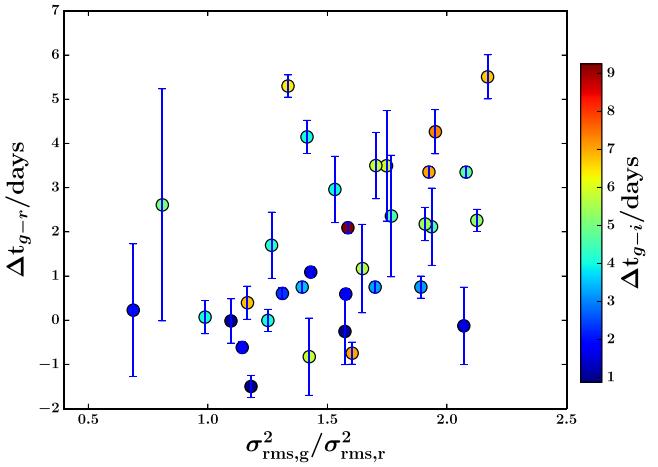


**Figure 15.** Correlation of $g-r$ lags ($\Delta t_{g-r}$) with the average ratio between the excess variance in the $g$ ($\sigma^2_{\rm rms,g}$) and $r$ ($\sigma^2_{\rm rms,r}$) bands for the 39 *cLD* quasars. Each data point is color coded by the $g-i$ lags ($\Delta t_{g-i}$).

probability distributions for the stacked lags for our sample are always positive as shown in Figure 10.

However, even in the subsample *cLD*, where well ordered lags with a single dominant peak are found, there are still four quasars with significantly negative values of $g-r$ lags as shown in the top panel of Figure 12, while the corresponding $g-i$ and $g-z$ lags are positive. We have also checked that when we measure the lags between $r$ and $i$ bands for these quasars, we find positive lags. Because quasars in each field have the same cadence, it will be hard to understand why only the four quasars in subsample *cLD* show significant negative lags if they are artifacts of the cadence or the failure of JAVELIN.

For the 63 quasars in subsample *iLD* having single dominant peaks but lags do not increase monotonically from $g-r$, $g-i$ to $g-z$, 14 of them have at least one significant negative lag, while 21 quasars have at least one band that does not follow this order significantly (at $2.35\sigma$ level).

To test the statistical significance of the number of quasars with unexpected, we randomly draw lag signals from 200 quasars by assuming Gaussian distributions with mean lags and standard deviations given by the stacked signals shown in Figure 10. At the $2.35\sigma$ level, there are no quasars with negative lags and there are only seven quasars with lags that do not increase monotonically. All of these numbers are much smaller than what we get from the data.

If these lags are physical signals, this suggests that there could still be drivers of the light-curve variability for these quasars located at the outer part of the disk where longer wavelength radiation is emitted. If the variability is caused by a driver at a particular radius and propagates outward, we expect the variation amplitude to decrease as the perturbation travels. In order to test the location of the driver, we calculate the normalized excess variance in the $g$ ($\sigma^2_{\rm rms,g}$) and $r$ bands ($\sigma^2_{\rm rms,r}$) in each season and calculate the mean ratio $\sigma^2_{\rm rms,g}/\sigma^2_{\rm rms,r}$ of the four observational seasons for each quasar in subsample *cLD*, which is plotted against the $g-r$ lags in Figure 15. There is a strong correlation between $\Delta t_{g-r}$ and $\sigma^2_{\rm rms,g}/\sigma^2_{\rm rms,r}$ with a Pearson correlation coefficient 0.43 with a corresponding $p$ value of 0.01 and a Spearman correlation coefficient of 0.47 with a corresponding $p$ value of 0.005. For the quasars with positive $\Delta t_{g-r}$, the fact that $\sigma^2_{\rm rms,g}/\sigma^2_{\rm rms,r}$ is larger as $\Delta t_{g-r}$ increases is consistent with the picture that the disturbance propagates from $g$ band to $r$ band and gets weaker as it travels. The further it propagates, the more the signal is damped. For the quasars with significant negative $\Delta t_{g-r}$, $\sigma^2_{\rm rms,g}/\sigma^2_{\rm rms,r}$ is smaller and gets close to 1. Particularly in the first season, we find that the ratio $\sigma^2_{\rm rms,g}/\sigma^2_{\rm rms,r}$ is smaller than 1 for these quasars. This is consistent with the suggestion that the driver is closer to the region where $r$-band radiation is emitted for the quasars with negative $g-r$ lags.

It is hard to understand the existence of these negative lags around the light crossing timescales in the context of the standard thin disk model, which predicts that the scale height of the radiation pressure dominated inner region of the black-hole accretion disk is a constant for different radii (Shakura & Sunyaev 1973). The X-ray and far-UV emission in quasars, which are thought to drive the variability, are believed to be produced by the corona on top of the accretion disk (e.g., Haardt & Maraschi 1991, 1993), and are also found to be located in a compact region near the innermost stable circular orbit (Chartas et al. 2009; Reis & Miller 2013). In order for an off-center region to produce significant variability, a special mechanism is required to operate at the $r$-band region and change the disk thickness there so that it can irradiate nearby radii. Recently, Jiang et al. (2016) pointed out that the iron opacity bump, which would exist around $1.8\times10^5$ K inside the disk, plays an important role to stabilize the accretion disks in AGNs and change the disk thickness. This is a promising mechanism because $r$-band radiation is expected to be emitted from a region around 26 Schwarzschild radii in our sample according to the estimate in Section 4.5, which is also the location where the iron opacity bump is expected. This mechanism also predicts significant outflows launched from this region, which can be tested with future observations.

Although only 16% of quasars in our sample have significant, well ordered lags for all $g$, $r$, $i$, $z$ bands individually, the stacked lags of the whole sample are all positive and increase with increasing wavelength differences. This is true even if we do not include subsample *cLD* during the stacking process. It suggests that this variability component, which is consistent with the picture of irradiation by the central source, exists for most quasars. However, for each individual quasar, this may not be the dominant component around the light crossing timescales. For example, strong off-center disturbances caused by localized regions around the iron opacity peak (Jiang et al. 2016) can be one candidate to cause the variability. Locations of the drivers in this case will change more significantly with black-hole mass and accretion rate, which may explain why these signals do not show up in the stacking process.

### 5.3. The Effects of Metallicity

It has been suggested that the line ratio Fe II/Mg II is a good proxy of metallicity in the broad line gas of quasars, and probably the accretion disk, although the uncertainty is large (Kurk et al. 2007; De Rosa et al. 2011). As the iron opacity bump will increase with higher metallicity, the modifications in disk structure compared with the standard thin disk model (Jiang et al. 2016) will be more significant, as long as the metallicity is larger than the solar value. Therefore, the inter-band lags may also show some correlation with the ratio between the equivalent widths of ultraviolet Fe II and Mg II, which is shown in Figure 16 for the subsample *cLD*. Despite

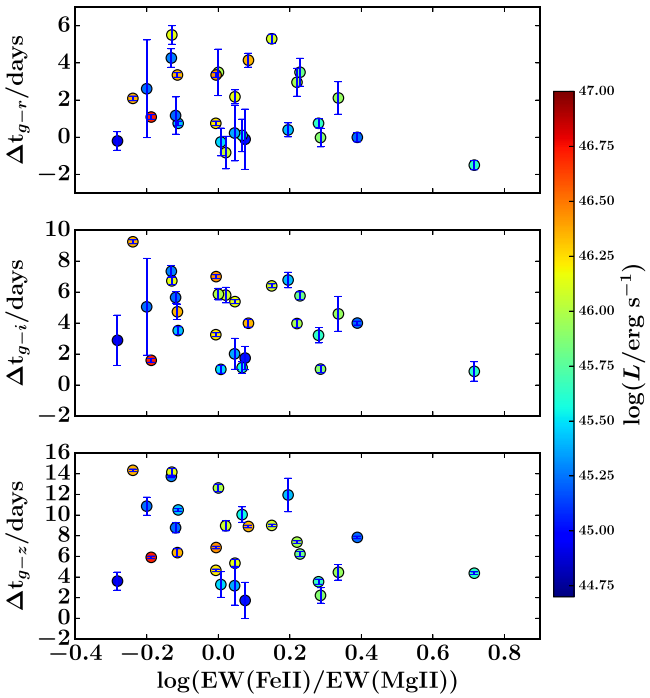


**Figure 16.** Correlation of the $g - r$ (top panel, $\Delta t_{g-r}$), $g - i$ (middle panel, $\Delta t_{g-i}$), and $g - z$ (bottom panel, $\Delta t_{g-z}$) lags with the ratio between the equivalent widths of ultraviolet Fe II and Mg II lines. Each data point is color coded with the bolometric luminosity.

large scatter, all three lags $\Delta t_{g-r}$, $\Delta t_{g-i}$, and $\Delta t_{g-z}$ show weak anti-correlations with EW(Fe II)/EW(Mg II), particularly when EW(Fe II)/EW(Mg II) is larger than 1. The Pearson correlation coefficients between the equivalent width ratio and $\Delta t_{g-r}$, $\Delta t_{g-i}$, $\Delta t_{g-z}$ are −0.34, −0.33, −0.30, while the corresponding Spearman correlation coefficients are −0.20, −0.28, and −0.35. The $p$ values for Pearson correlation coefficients are 0.07, 0.08, and 0.11. Each data point is color coded by luminosity in Figure 16, which shows no clear trend between luminosity and the equivalent ratio. This suggests that the anti-correlation between lag and EW(Fe II)/EW(Mg II) is independent of the weak correlation between lag and luminosity shown in Figure 12. If the equivalent width ratio is a good indicator of metallicity, this indeed suggests that at large enough metallicity, the structure of the disk may change and affect the inter-band lags. However, more theoretical studies are clearly needed to understand each type of lag behavior as described in Section 4.1.

### 5.4. Uncertainties in the Thin Disk Model

There are still some uncertainties in the simple disk model we compare to that may affect the predicted lags in Equation (2). The parameter $f_i$ represents the heating of the disk by the central radiation. We set it to 1 for simplicity,[17] which means the disk temperature is still determined by the local viscous heating. Because the lags are only proportional to $f_i^{1/3}$, in order to make the predicted lags three times larger, $f_i$ needs to be increased to 27, which means the disk temperature is completely determined by the irradiation. However, this is unlikely, particularly in the outer part of the disk because the central radiation flux will drop with distance $R$ as $R^{-3}$ in the lamp post model with a thin disk geometry. There is also no reason to believe that the disk temperature will have the same radial profile as in the standard thin disk model, which is what we assume in Equation (2). The predicted lags also have a weak dependence on the black-hole mass. If the discrepancy is caused by errors in the estimated black-hole mass, the masses of all the quasars need to be systematically underestimated by a factor of 27 in order to increase the predicted lags by a factor of three. Although the single-epoch virial method we use to estimate the black-hole mass is very uncertain, the systematic error is unlikely to be so large (Shen 2013). If the black-hole mass increased by a factor of 27, there would be many black holes with mass larger than $10^{10}\,M_\odot$ and the Eddington ratios for most of the quasars would be smaller than ∼1%, neither of which is likely. The inclination of the disk will also change the line-of-sight distance at different locations of the disk. On the near side of the disk, the outer part of the disk is closer to us while on the far side of the disk, the inner part is closer to us. This will just broaden the lag signals and the mean lag values will be unaffected (Starkey et al. 2016).

[17] The parameter $f_i$ is equivalent to $1 + \kappa/3$ in Fausnaugh et al. (2016), which was chosen to be $4/3$.

### 5.5. Extension to Different Redshifts

We selected particular redshift ranges to avoid significant contamination by broad emission lines in the Pan-STARRS filters. This also limits the size of our sample and the radial range of the accretion disks we can probe. In principle, when we fit the light curves based on DRW models, we can use more than one component in each band to fit both the continuum and lines simultaneously. A similar technique has been demonstrated by Chelouche & Zucker (2013; see also Zu et al. 2016) to separate the continuum–continuum and continuum–line lags. In this way, lags of quasars in different redshift ranges can be studied. We will apply this technique to the Pan-STARRS data in the near future.

## 6. Summary

In summary, we have used more than four years of light curves from the Pan-STARRS MDFs to detect continuum-band lags in 200 quasars. The mean lags between the $g$ band and the $r$, $i$, and $z$ bands for the whole sample are 1.1, 2.1, and 3.0 days. There are 39 quasars showing significantly detected lags that increase toward redder bands, as expected if the lags correspond to the light crossing times across different radii of the accretion disks when the outer part of the disk is irradiated by the central source. The detected lags are systematically larger than the expected values based on the standard thin disk models by a factor of 2–3, which cannot be explained by uncertainties in the measurements (for example, black-hole mass) or the thin disk model (for example, the inclination). The stacked lags and theoretically expected values are summarized in Figure 17. This is consistent with the recent results for NGC 5548 and microlensing measurements. The correlations between the $g - r$, $g - i$, and $g - z$ lags are also significantly different from thin disk model predictions, particularly for quasars with larger lags and higher luminosities.

The detected lags are found to increase with increasing luminosity, which is also clearly shown in Figure 17. This is probably because accretion disk sizes are larger for high-luminosity quasars. We also find evidence that the lags decrease with increasing ratio EW(Fe II)/EW(Mg II), particularly when this ratio is large. This may indicate that the accretion disk

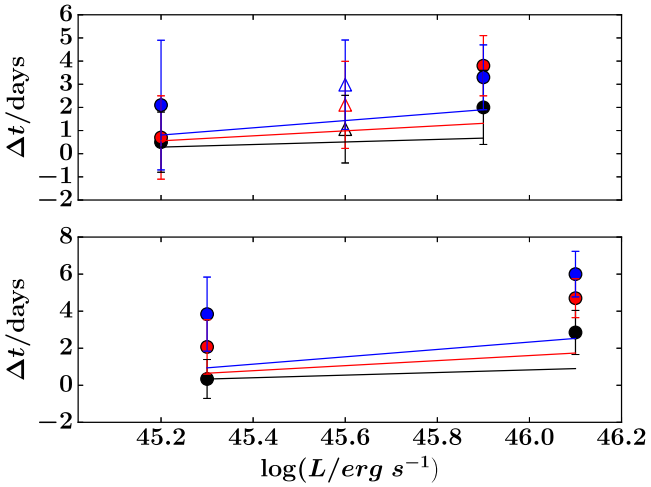


**Figure 17.** Top: summary of the stacked lag signals with median luminosity for the whole sample. The open black, red, and blue triangles are the stacked $g-r$, $g-i$, and $g-z$ lags as shown in Figure 10. The filled black, red, and blue circles are the stacked $g-r$, $g-i$, and $g-z$ lags for two luminosity bins with the theoretically expected values for each luminosity bin connected by the black, red, and blue lines. Bottom: the corresponding stacked lags of the subsample *cLD* for two luminosity bins as shown in Figure 13.

structure is changed in quasars with higher metallicity, probably because of the effects of the iron opacity bump (Jiang et al. 2016). There are also four quasars in subsample *cLD* with significant negative lags between the $g$ and $r$ bands and we find the correlation that the ratios between the excess variance in $g$ and $r$ bands generally increase with increasing $g-r$ lags. This indicates that some quasars may have strong off-center variability that will complicate the lag signals.

It will be interesting to carry out the same experiment with more data at different redshifts, which will allow us to probe a larger radial range of the accretion disk. For the quasars with lags that are consistent with the lamp post model, the Continuum Reprocessed AGN Markov Chain Monte Carlo (CREAM; Starkey et al. 2016) model can be used to constrain the properties of the accretion disks (such as inclination and mass-accretion rate). The correlations we find between the lags and physical properties of the accretion disks will be significantly improved with better sampled data and more quasars. This will be one interesting application of LSST data. Better data with regular approximately one-day cadence will also be able to tell whether the lags with unexpected orders are physical or not.

Y.F.J. and A.P. are supported by NASA through Einstein Postdoctoral Fellowship grant number PF3-140109 and PF5-160141 awarded by the *Chandra* X-ray Center. Y.S. acknowledges support from an Alfred P. Sloan Research Fellowship and W.N.B. acknowledges support from NSF grant AST-1516784.

The Pan-STARRS1 Surveys (PS1) have been made possible through contributions by the Institute for Astronomy, the University of Hawaii, the Pan-STARRS Project Office, the Max-Planck Society and its participating institutes, the Max Planck Institute for Astronomy, Heidelberg and the Max Planck Institute for Extraterrestrial Physics, Garching, The Johns Hopkins University, Durham University, the University of Edinburgh, the Queen's University Belfast, the Harvard-Smithsonian Center for Astrophysics, the Las Cumbres Observatory Global Telescope Network Incorporated, the National Central University of Taiwan, the Space Telescope Science Institute, and the National Aeronautics and Space Administration under Grant No. NNX08AR22G issued through the Planetary Science Division of the NASA Science Mission Directorate, the National Science Foundation Grant No. AST-1238877, the University of Maryland, Eotvos Lorand University (ELTE), and the Los Alamos National Laboratory.

Funding for SDSS-III has been provided by the Alfred P. Sloan Foundation, the Participating Institutions, the National Science Foundation, and the U.S. Department of Energy Office of Science. The SDSS-III web site is http://www.sdss3.org/.

SDSS-III is managed by the Astrophysical Research Consortium for the Participating Institutions of the SDSS-III Collaboration including the University of Arizona, the Brazilian Participation Group, Brookhaven National Laboratory, Carnegie Mellon University, University of Florida, the French Participation Group, the German Participation Group, Harvard University, the Instituto de Astrofisica de Canarias, the Michigan State/Notre Dame/JINA Participation Group, The Johns Hopkins University, Lawrence Berkeley National Laboratory, Max Planck Institute for Astrophysics, Max Planck Institute for Extraterrestrial Physics, New Mexico State University, New York University, The Ohio State University, Pennsylvania State University, University of Portsmouth, Princeton University, the Spanish Participation Group, University of Tokyo, University of Utah, Vanderbilt University, University of Virginia, University of Washington, and Yale University.

## References

Ai, Y. L., Yuan, W., Zhou, H. Y., et al. 2010, ApJL, 716, L31
Alam, S., Albareti, F. D., Allende Prieto, C., et al. 2015, ApJS, 219, 12
Barth, A. J., Bennert, V. N., Canalizo, G., et al. 2015, ApJS, 217, 26
Bauer, A., Baltay, C., Coppi, P., et al. 2009, ApJ, 696, 1241
Bentz, M. C., Walsh, J. L., Barth, A. J., et al. 2009, ApJ, 705, 199
Blandford, R. D., & McKee, C. F. 1982, ApJ, 255, 419
Breedt, E., Arévalo, P., McHardy, I. M., et al. 2009, MNRAS, 394, 427
Breedt, E., McHardy, I. M., Arévalo, P., et al. 2010, MNRAS, 403, 605
Cackett, E. M., Horne, K., & Winkler, H. 2007, MNRAS, 380, 669
Chartas, G., Kochanek, C. S., Dai, X., Poindexter, S., & Garmire, G. 2009, ApJ, 693, 174
Chartas, G., Rhea, C., Kochanek, C., et al. 2016, AN, 337, 356
Chelouche, D., & Zucker, S. 2013, ApJ, 769, 124
Choi, Y., Gibson, R. R., Becker, A. C., et al. 2014, ApJ, 782, 37
Collier, S. J., Horne, K., Kaspi, S., et al. 1998, ApJ, 500, 162
Dawson, K. S., Schlegel, D. J., Ahn, C. P., et al. 2013, AJ, 145, 10
De Rosa, G., Decarli, R., Walter, F., et al. 2011, ApJ, 739, 56
Dexter, J., & Agol, E. 2011, ApJL, 727, L24
Edelson, R., Gelbord, J. M., Horne, K., et al. 2015, ApJ, 806, 129
Eisenstein, D. J., Weinberg, D. H., Agol, E., et al. 2011, AJ, 142, 72
Ellaway, P. H. 1978, Electroencephalogr. Clin. Neurophysiol., 45, 302
Fausnaugh, M. M., Denney, K. D., Barth, A. J., et al. 2016, ApJ, 821, 56
Gardner, E., & Done, C. 2016, arXiv:1603.09564
Haardt, F., & Maraschi, L. 1991, ApJL, 380, L51
Haardt, F., & Maraschi, L. 1993, ApJ, 413, 507
Janiuk, A., Czerny, B., & Siemiginowska, A. 2002, ApJ, 576, 908
Jiang, Y.-F., Davis, S., & Stone, J. 2016, ApJ, 827, 10
Jiang, Y.-F., Stone, J. M., & Davis, S. W. 2013, ApJ, 778, 65
Kelly, B. C., Bechtold, J., & Siemiginowska, A. 2009, ApJ, 698, 895
Kim, D.-W., Protopapas, P., Byun, Y.-I., et al. 2011, ApJ, 735, 68
Koratkar, A., & Blaes, O. 1999, PASP, 111, 1
Kozłowski, S. 2016, ApJ, 826, 118
Kozłowski, S., Kochanek, C. S., Udalski, A., et al. 2010, ApJ, 708, 927
Krolik, J. H., Horne, K., Kallman, T. R., et al. 1991, ApJ, 371, 541
Kurk, J. D., Walter, F., Fan, X., et al. 2007, ApJ, 669, 32
Laor, A., & Davis, S. W. 2014, MNRAS, 438, 3024
Lawrence, A. 2012, MNRAS, 423, 451
Lawrence, A. 2016, ASPC, 505, 107
Lira, P., Arévalo, P., Uttley, P., McHardy, I., & Breedt, E. 2011, MNRAS, 415, 1290

MacLeod, C. L., Ivezić, Ž., Kochanek, C. S., et al. 2010, ApJ, 721, 1014
Marshall, K., Ryle, W. T., & Miller, H. R. 2008, ApJ, 677, 880
McHardy, I. M., Cameron, D. T., Dwelly, T., et al. 2014, MNRAS, 444, 1469
McHardy, I. M., Connolly, S. D., Peterson, B. M., et al. 2016, AN, 337, 500
Morgan, C. W., Kochanek, C. S., Morgan, N. D., & Falco, E. E. 2010, ApJ, 712, 1129
Morganson, E., Green, P. J., Anderson, S. F., et al. 2015, ApJ, 806, 244
Mosquera, A. M., Kochanek, C. S., Chen, B., et al. 2013, ApJ, 769, 53
Nandra, K., George, I. M., Mushotzky, R. F., Turner, T. J., & Yaqoob, T. 1997, ApJ, 476, 70
Pâris, I., Petitjean, P., Aubourg, É, et al. 2014, A&A, 563, A54
Peterson, B. M. 1993, PASP, 105, 247
Peterson, B. M., Ferrarese, L., Gilbert, K. M., et al. 2004, ApJ, 613, 682
Peterson, B. M., Wanders, I., Horne, K., et al. 1998, PASP, 110, 660
Ponti, G., Papadakis, I., Bianchi, S., et al. 2012, A&A, 542, A83
Reis, R. C., & Miller, J. M. 2013, ApJL, 769, L7
Schlafly, E. F., Finkbeiner, D. P., Jurić, M., et al. 2012, ApJ, 756, 158
Sergeev, S. G., Doroshenko, V. T., Golubinskiy, Y. V., Merkulova, N. I., & Sergeeva, E. A. 2005, ApJ, 622, 129
Shakura, N. I., & Sunyaev, R. A. 1973, A&A, 24, 337
Shakura, N. I., & Sunyaev, R. A. 1976, MNRAS, 175, 613
Shappee, B. J., Prieto, J. L., Grupe, D., et al. 2014, ApJ, 788, 48
Shen, Y. 2013, BASI, 41, 61
Shen, Y., Brandt, W. N., Dawson, K. S., et al. 2015, ApJS, 216, 4
Shen, Y., Horne, K., Grier, C. J., et al. 2016, ApJ, 818, 30
Shen, Y., Richards, G. T., Strauss, M. A., et al. 2011, ApJS, 194, 45
Shields, G. A. 1978, Natur, 272, 706
Simm, T., Salvato, M., Saglia, R., et al. 2016, A&A, 585, A129
Starkey, D. A., Horne, K., & Villforth, C. 2016, MNRAS, 456, 1960
Stubbs, C. W., Doherty, P., Cramer, C., et al. 2010, ApJS, 191, 376
Telfer, R. C., Zheng, W., Kriss, G. A., & Davidsen, A. F. 2002, ApJ, 565, 773
Tonry, J. L., Stubbs, C. W., Lykke, K. R., et al. 2012, ApJ, 750, 99
Troyer, J., Starkey, D., Cackett, E. M., et al. 2016, MNRAS, 456, 4040
Uttley, P., Edelson, R., McHardy, I. M., Peterson, B. M., & Markowitz, A. 2003, ApJL, 584, L53
Vaughan, S., Edelson, R., Warwick, R. S., & Uttley, P. 2003, MNRAS, 345, 1271
Wanders, I., Peterson, B. M., Alloin, D., et al. 1997, ApJS, 113, 69
Welsh, W. F. 1999, PASP, 111, 1347
Wilhite, B. C., Brunner, R. J., Grier, C. J., Schneider, D. P., & vanden Berk, D. E. 2008, MNRAS, 383, 1232
Zu, Y., Kochanek, C. S., Kozłowski, S., & Peterson, B. M. 2016, ApJ, 819, 122
Zu, Y., Kochanek, C. S., & Peterson, B. M. 2011, ApJ, 735, 80